HHS Public Access

Author manuscript

Immunity. Author manuscript; available in PMC 2024 November 06.

Published in final edited form as:

Immunity. 2024 June 11; 57(6): 1306–1323.e8. doi:10.1016/j.immuni.2024.05.004.

Intestinal ILC3s Migrate to the Kidney and Promote Renal Fibrosis via PD-1-mediated Activation

Zhou Liang[1,2,12], **Ziwen Tang**[1,2,12], **Changjian Zhu**[1,2,12], **Feng Li**[1,2], **Shuaijiabin Chen**[3], **Xu Han**[1,2], **Ruilin Zheng**[1,2], **Xinrong Hu**[1,2], **Ruoni Lin**[1,2], **Qiaoqiao Pei**[1,2], **Changjun Yin**[4], **Ji Wang**[4], **Ce Tang**[4], **Nan Cao**[5], **Jincun Zhao**[6], **Rong Wang**[1,2], **Xiaoyan Li**[1,2], **Ning Luo**[1,2], **Qiong Wen**[1,2], **Jianwen Yu**[1,2], **Jianbo Li**[1,2], **Xi Xia**[1,2], **Xunhua Zheng**[1,2], **Xin Wang**[1,2], **Naya Huang**[1,2], **Zhong Zhong**[1,2], **Chengqiang Mo**[7], **Peisong Chen**[8], **Yating Wang**[1,2], **Jinjin Fan**[1,2], **Yun Guo**[1,2], **Haojie Zhong**[1,2], **Jiaqi Liu**[1,2], **Zhenwei Peng**[9], **Haiping Mao**[1,2], **Guo-Ping Shi**[10], **Joseph V. Bonventre**[11,*], **Wei Chen**[1,2,*], **Yi Zhou**[1,2,13,*]

[1]Department of Nephrology, The First Affiliated Hospital, Sun Yat-sen University, Guangzhou, 510080, China

[2]NHC Key Laboratory of Clinical Nephrology (Sun Yat-sen University) and Guangdong Provincial Key Laboratory of Nephrology, Guangzhou, 510080, China

[3]State Key Laboratory of Membrane Biology, Beijing Advanced Innovation Center for Structural Biology, Beijing Frontier Research Center for Biological Structure, School of Life Sciences, Tsinghua University, Beijing, 100084, China

[4]Precision Medicine Research Center, The First Affiliated Hospital, Sun Yat-sen University, Guangzhou, 510080, China

[5]Key Laboratory for Stem Cells and Tissue Engineering (Sun Yat-Sen University), Ministry of Education, Guangzhou, 510080, China

[6]State Key Laboratory of Respiratory Disease, National Clinical Research Center for Respiratory Disease, Guangzhou Institute of Respiratory Health, The First Affiliated Hospital of Guangzhou Medical University, Guangzhou, 510182, China

[7]Department of Urology, The First Affiliated Hospital of Sun Yat-sen University, Guangzhou, 510080, China

[8]Department of Laboratory Medicine, The First Affiliated Hospital, Sun Yat-sen University, Guangzhou, 510080, China

[*]Correspondence: zhouyi39@mail.sysu.edu.cn (Y.Z.); chenwei99@mail.sysu.edu.cn (W.C.); jbonventre@bwh.harvard.edu (J.V.B.).

AUTHOR CONTRIBUTIONS

Z.L., Z.T., C.Z., W.C. and Y.Z. designed, performed and interpreted all experiments. Z.L., Z.T., C.Z., and F.L. carried out data analysis. Z.L. and Z.T. performed all bioinformatics analysis. Z.L., Z.T., C.Z., F.L., R.W., X.Han., R.Z., X.Hu., R.L., Q.P., H.Z., J.Liu. and Y.G. performed all animal work. X.L., N.L. and J.F. performed kidney primary fibroblast cell isolation and culture. S.C. performed protein structure prediction. X.Z. and J.Y., collected clinical blood samples from patients. P.C. collected blood samples from health controls. J.Y., Q.W., J.Li., X.X., X.Z., X.W., N.H. and Z.Z. collected kidney biopsies from patients. C.M. collected kidney biopsies from health controls. H.M. and Y.W. provided technical assistance with fibrosis analysis. J.V.B., C.Y., J.W., C.T., N.C., Z.P., G.P.S. and J.Z. interpreted experiments, carried out data analysis and/or provided reagents. Z.L., Z.T., C.Z., J.V.B., W.C., and Y.Z. wrote the manuscript.

DECLARATION OF INTERESTS

The authors declare no competing interests.

[9]Department of Radiation Oncology, The First Affiliated Hospital, Sun Yat-sen University, Guangzhou, 510080, China

[10]Department of Medicine, Brigham and Women's Hospital, Harvard Medical School, Boston, MA 02115, USA

[11]Department of Nephrology, Brigham and Women's Hospital, Harvard Medical School, Boston, MA 02115, USA

[12]These authors contributed equally

[13]Lead contact

SUMMARY

Group 3 innate lymphoid cells (ILC3s) are enriched in mucosa, regulating inflammation and tissue repair, yet their role in renal fibrosis remains unclear. Here, we reported that renal fibrosis and dysfunction were associated with increased ILC3s in human kidneys and blood. Using murine models, we showed that the rapidly accumulated ILC3s in the kidney primarily originated from the intestinal mucosa. $CXCR6^+$ ILC3s were migrated to the kidney by the chemokine CXCL16 released from the injured tubules. Within the fibrotic kidney, ILC3s increased the expression of programmed death receptor-1 (PD-1) to directly activate myofibroblasts and fibrotic niche formation by producing IL-17A. PD-1 inhibition of IL-23R endocytosis and consequent amplification of JAK2/STAT3/RORγt/IL-17A pathway was essential for the pro-fibrogenic effect of ILC3s. Thus, we reveal a hitherto unrecognized migration pathway of ILC3s from the intestine to the kidney and the PD-1-dependent function of ILC3s in promoting renal fibrosis.

Graphical Abstract

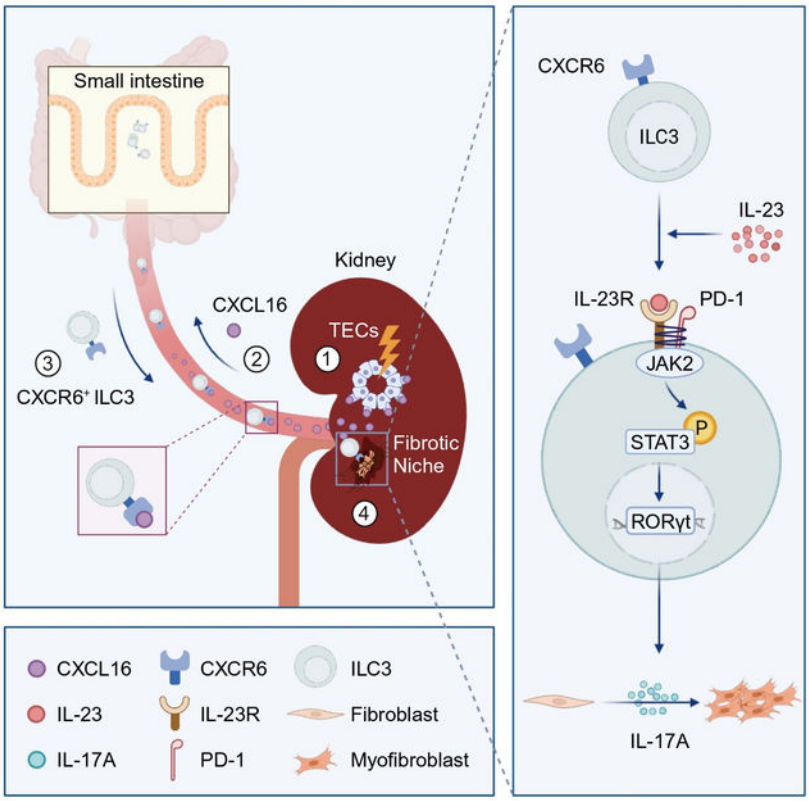

INTRODUCTION

Innate lymphoid cells (ILCs) are heterogeneous lymphocytes that lack rearranged antigen receptors and react to insults through cytokine production, initiating critical immune responses and tissue repair.[1–5] Group 3 innate lymphoid cells (ILC3s) require expression of retinoid-related orphan receptor γt (RORγt), produce IL-17A and/or IL-22, and are abundant in mucosal barrier sites like the small intestine.[1] ILC3s also reside in parenchymal organs such as the liver and kidney.[6–10] ILC3s function in both physiological and pathological processes, including maintenance of mucosal homeostasis, tissue repair, resistance to bacterial infection, and tumor immune surveillance.[8,11–13] ILC3s can promote fibrogenesis in intestines infected with *Salmonella* and in CCl4-induced murine liver fibrosis via IL-17A/IL-22 production, indicating a role in fibrotic remodeling.[6,10,14] However, whether ILC3s are involved in renal fibrosis remains unclear.

Renal fibrosis is the common fate for nearly all types of chronic kidney disease (CKD).[15,16] In response to multiple stimuli, immune cells infiltrate the kidney at a very early stage, producing proinflammatory mediators that directly induce fibroblasts to differentiate into alpha-smooth muscle actin (α-SMA)-expressing myofibroblasts. This ultimately causes aberrant extracellular matrix (ECM) deposition and irreversible structural and functional damage.[17–21] Given that IL-23, IL-1β, and IL-17A are important proinflammatory cytokines in CKD[22–24] and are major regulatory mediators and effectors of ILC3s,[25] we hypothesized that ILC3s may be involved in renal fibrosis.

In this study, we showed that ILC3s were rapidly recruited to the kidneys from the small intestines via CXCR6/CXCL16 signaling, and promoted renal fibrosis by activating fibroblasts and initiating fibrogenic niche formation. Mechanistically, the profibrogenic roles of ILC3s depended on programmed cell death-1 (PD-1) expression, which was induced by IL-23/IL-1β in the renal fibrotic microenvironment. PD-1 bound to IL-23R and inhibited its endocytosis, thereby maintaining IL-23R on the surface of ILC3s and amplifying downstream intracellular JAK2/STAT3/RORγt signaling and subsequent IL-17A secretion. Ultimately, increased IL-17A drove ECM production by renal fibroblasts. A similar pattern was also detected in CKD patients, supporting the translational potential of these discoveries. Our data show the unique contribution of ILC3s in renal fibrogenesis via likely the intestine-kidney connection. Furthermore, targeting ILC3s gut-kidney migration or PD-1 in renal ILC3s has therapeutic potential to prevent CKD.

RESULTS

ILC3s accumulate in human and mouse renal fibrosis

To evaluate the correlation of ILCs with renal fibrosis progression, we performed immunofluorescence staining in kidney biopsies of CKD patients with $CD3^{-}CD127^{+}$ ILCs[26] and fibrosis indicator α-SMA. Kidney specimens were divided into different regions according to the extent of fibrosis. ILCs were mainly located in the fibrotic areas, and their density positively correlated with α-SMA expression (Figures 1A, S1A, and S1B). Various immune cells – including macrophages, T cells, B cells, dendritic cells (DCs), and neutrophils – affect fibrotic kidneys.[17,18,20,27] We therefore analyzed these immune cells along with ILCs in kidney specimens from the same cohort (Figures S1C and S1D). Despite relatively lower absolute numbers of ILCs compared to other immune populations (Figure S1E), their fibrosis-associated increase was second only to macrophages and exceeded T cells, B cells, DCs, and neutrophils (Figures 1B and S1F), representing an important association between ILCs and renal fibrosis.

We next analyzed fresh tissue specimens from CKD kidney biopsies (Table S1) using a validated flow cytometry panel (Figure S1G). Within the $CD45^{+}LIN^{-}CD127^{+}$ lymphocytes, ILC subsets were identified as $ROR\gamma t^{+}$ ILC3s, $CD56^{-}ROR\gamma t^{-}CRTH2^{+}$ ILC2s, $CD56^{-}ROR\gamma t^{-}CRTH2^{-}CD117^{-}$ ILC1s, and $CD56^{-}ROR\gamma t^{-}CRTH2^{-}CD117^{+}$ ILC precursors (ILCps). The collective ILC population was quantified by aggregating ILC1s, ILC2s, ILC3s, and ILCps. The proportion of ILCs in leukocytes was elevated in CKD patients' kidneys compared with healthy controls (HCs) (~ 0.6% *vs.* ~ 1.5%) (Figure 1C). Among ILC subsets, in kidneys of HCs or CKD patients without renal fibrosis, ILC2 was the most dominant ILC subset. Surprisingly, however, in CKD patients who developed renal fibrosis, the proportions of ILC subgroups shifted, making ILC3 the predominant subset (from 7.7 ~ 10.2% in normal or non-fibrosis to ~ 36.7% in fibrosis) (Figures 1D and 1E). We also analyze ILC subsets in the peripheral blood mononuclear cells (PBMCs) in a cohort of 80 CKD patients and 16 HCs, based on the same panel (Table S2 and Table S3). Like the kidney, circulating ILC3 frequency increased in CKD patients with renal fibrosis compared to non-fibrotic organs or HCs, and was negatively associated with patients' renal function as measured by the estimated glomerular filtration rate (eGFR) (Figures 1F–1H).

Immunofluorescence co-staining identified that kidney CD3^{-}RORγt^{+} ILC3s were increased within fibrotic lesions and correlated with α-SMA intensity (Figure 1I). These data raise the possibility that circulating- and kidney-ILC3s may contribute to renal fibrogenesis.

To further characterize ILC3s, we established two classic mouse models of renal fibrosis, unilateral ureteral obstruction (UUO) of surgically induced progressive renal fibrosis, and folic acid nephropathy (FAN) prone to chronic onset and progression.[28–31] Consistent with the human data, both blood- and kidney-ILC3s markedly increased at day 3 (UUO3d, early fibrosis) and day 14 (UUO14d, late fibrosis) after UUO compared to the sham-operated group (Figure 1J). ILC3s were elevated in folic acid (FA)-induced fibrotic kidneys as well (Figure 1K). Similarly, mouse kidney ILC3s were also enriched within fibrotic niches, where ILC3 density correlated with α-SMA expression and loss of renal function, as reflected by serum creatinine levels and blood urea nitrogen (BUN) (Figures 1L–1Q). Additionally, ILC3 aggregation within injured tissues was observed in an ischemia-reperfusion injury (IRI)-induced fibrosis mouse model (Figure S1H).[31] Altogether, these results demonstrate that both human and experimental murine models manifested substantial accumulation of ILC3s, primarily within kidney fibrotic niche structures.

Intestine-derived ILC3s rapidly accumulate in fibrotic kidney

To investigate the dynamic accumulation of ILCs during renal fibrosis, we analyzed their changes at different time points after UUO by flow cytometry and compared them with other immune cells. ILC numbers increased 5-fold as early as 6 hours post-surgery, outpacing T/B lymphocyte infiltration, though less than macrophages and neutrophils. Moreover, ILC numbers maintained rapid growth in the first 3 days and continued to increase as fibrosis proceeded in UUO mice (Figure S2A).

ILC3s are considered tissue-resident cells, however they can also migrate between organs.[32] To determine the origin of increased kidney ILC3s during fibrosis, we stained proliferation marker Ki67 and resident cell markers CD69, CD103, and CD49a[33,34] on ILC3s by immunofluorescence and flow cytometry, examining whether they were proliferative renal-resident cells. The results showed that only a minimal fraction of ILC3s in UUO kidneys harbored those markers (Figures 2A and 2B), suggesting limited local proliferation. In addition, ILC3s were predominantly located in fibrogenic niches around blood vessels where circulating cells enter tissue parenchyma (Figure 2C), implying the extrarenal origin of kidney ILC3s.

To define the source of renal ILC3s, we investigated ILC3s in different organs during UUO, including the kidney, PBMC, small intestine (SI), lung, spleen, and bone marrow (BM). Flow cytometry analysis revealed a substantial elevation of ILC3s in UUO kidneys and a lesser extent in PBMC, lung, and spleen, while conversely, a robust decrease of ILC3s in SI (Figure 2D), which was also observed in FAN mice (Figure 2E). This concurrent rise and fall between the kidney and intestine suggests that ILC3s in fibrotic kidney may migrate from SI.

We next utilized Kaede photo-convertible reporter mice[35] to further examine the gut-kidney trafficking of ILC3s during fibrosis. Before UUO surgery, *Kaede* transgenic mice received

UV illumination strictly confined to SI (Figures 2F and S2B), where the tissue photo-converted from green to red fluorescence and immune cells were effectively labeled with red signals (Figures S2C–S2E). We found that intestine-labeled Kaede-red cells were observed in kidney sections (Figure 2G), and the majority of ILC3s in fibrotic kidneys were detected as Kaede-red$^+$ cells by flow cytometry (Figure 2H), demonstrating that kidney-infiltrating ILC3s migrated from the intestines. Complementing the elevation of ILC3s detected in multiple tissues, varying amounts of Kaede-red$^+$ intestinal ILC3s were also found in these peripheral organs and lymph nodes, but all at significantly lower frequencies than in the kidney (0.3% ~ 17.6% *vs.* 72.1%) (Figures S2F and 2H). These results thus support multi-tissue trafficking of intestinal ILC3s during renal fibrosis, with predominantly gut-kidney migration occurring.

Further unbiased analysis of photoconverted cells in injured kidneys revealed that in addition to ILCs, different types of Kaede-red$^+$ intestinal immune cells could be detected in kidneys (Figure 2I). Kaede-red$^+$ ILCs accounted for approximately 63.9% of the total renal ILCs, whereas the frequencies of Kaede-red$^+$ in other renal immune cells were limited (2 ~ 8.4%). Also, when considering the composition of Kaede-red$^+$ cells in kidney, ILCs constituted the largest fraction, about 36.2% (Figure 2J). Again, the vast majority of Kaede-red$^+$ ILCs were identified as ILC3s (~ 63.2%). Altogether, these data indicate that during kidney injury, gut-kidney migration of ILCs appears to be more specific than other immune cells, with ILC3s being the prominent cell type originating from the intestine.

Intestinal ILC3s migrate into injured kidney via CXCR6-CXCL16 axis

To explore the mechanisms underlying ILC3 migration, we performed single-cell RNA sequencing (scRNA-seq) analyses of renal and intestinal ILCs isolated from UUO mice at different disease stages (Figures 3A and S3A). Intestinal ILCs in UUO0d and UUO3d represented ILCs in “steady state (pre-migration)” and “mobilization state (post-migration)” respectively; renal ILCs from UUO3d and UUO14d represent “early fibrosis” and “late fibrosis” respectively. All samples were validated abundant expression of ILC-related transcripts as previously described,[36,37] alongside low expression of specific transcripts related to other cellular lineages (Figure S3B). ILC subsets were visualized by Uniform Manifold Approximation and Projection (UMAP) (Figure 3B). Evolution trajectories of ILC3s plotted with Monocle[38] showed that intestinal cells predominantly stayed in the initial stage of the trajectory, then bifurcated into two diverse branches — one progressed toward renal ILC3s and another maintained intestinal gene expression (Figure 3C). This suggested that renal ILC3s originate from intestinal ILC3s.

Given that ILC migration is primarily driven by chemokines and their corresponding chemokine receptors,[39–41] we thus profiled chemokine receptors between cells from the two tissues and revealed that both renal and intestinal ILC3s highly expressed *Cxcr6* and *Cxcr4* (Figure 3D). We subsequently validated CXCR6-expressing ILC3s to be the predominant population in both tissues during UUO (Figure 3E) with comparable CXCR6 protein expression levels (Figure 3F). Moreover, we detected increased tissue expression of its unique ligand CXCL16 on injured tubules (Figures 3G, 3H, S3C, and S3D) and concomitant elevation of serum secretory CXCL16 (sCXCL16) (Figures 3I and 3J) in renal

fibrosis mice and CKD patients. Serum sCXCL16 correlated with ILC3 numbers in kidney and circulation (Figures 3K and 3L), suggesting that intestinal CXCR6^{+} ILC3s migration could be driven by renal expression and release of CXCL16 into circulation.

To ascertain whether CXCR6/CXCL16 axis is involved in ILC3s trafficking, we conducted CXCL16-blockade experiments using wild-type (WT) and *Kaede* transgenic mice, respectively (Figure 3M). Pharmacological inhibition of CXCL16 inhibited ILC3s accumulation in the kidney (Figures 3N and S3E) and simultaneously recovered ILC3s in the intestine (Figures 3O and S3F). Parallelly, in *Kaede*-UUO mice, renal Kaede-red^{+} ILC3s were reduced after blocking CXCL16 (Figure 3P), affirming that CXCL16 blockade could effectively inhibit ILC3 gut-kidney migration. Next, employing CXCR6-deficient mice (*Cxcr6*$^{gfp/gfp}$), we demonstrated that ILC3s in *Cxcr6*$^{gfp/gfp}$-UUO intestines did not decline as observed in WT-UUO (Figures 3Q, S3G, and 2D). Alternatively, we transferred sorted WT-ILC3s or *Cxcr6*$^{gfp/gfp}$-ILC3s into UUO mice. Contrary to the increase of renal ILC3s in WT-ILC3s-recipient, mice receiving *Cxcr6*$^{gfp/gfp}$-ILC3s did not experience any elevation in ILC3 numbers and frequencies (Figures 3R, 3S, and S3H), confirming the necessity of CXCR6 for ILC3 gut-kidney migration. Together, these findings demonstrate that ILC3s emigrate out of the intestine and migrate into the fibrotic kidney via CXCR6/CXCL16 axis.

When comparing CXCR6 expression across various immune cells in the intestine, ILCs (~ 72.3%), and particularly ILC3s (96.4%), had the highest proportion of CXCR6^{+} cells (Figures S3I and S3J). Consistently, *Kaede* transgenic mice further verified that renal axial migration of immune cells matched their respective CXCR6 levels and was blocked by CXCL16 neutralization (Figure S3K). ILCs served as the most responsive to this chemotactic axis and therefore were more readily recruited to the injured kidney.

ILC3s mediate fibrotic niche formation and contribute to renal fibrosis

Infiltrating ILC3s within human and mouse kidneys selectively located within the well-formed α-SMA^{+} aggregates (resembling fibrogenic niche structures) (Figures 1I, 1L, and 1O), suggesting potential roles for ILC3s in fibrotic niche formation. To elucidate the *in vivo* function of these migrated ILC3s, we examined renal fibrosis following CXCL16-neutralization, and found that CXCL16 blockade attenuated α-SMA expression and ECM deposition of collagen I and fibronectin in UUO kidneys (Figure S4A). Thus, disrupting the ILC3 gut-kidney migration alleviated renal fibrosis.

Furthermore, we assessed the impact of ILC3 deletion on UUO kidneys. Since *Rorc*$^{-/-}$ mice lack RORγt, which is essential for ILC3s and Th17 cells,[42] we implemented a chimeric mouse strategy to rule out the impact of Th17 cells.[43] Briefly, BM from WT (Th17 cells^{+}ILC3s^{+}), *Rorc*$^{-/-}$(Th17 cells^{-}ILC3s^{-}), and a mix of *Rag1*$^{-/-}$ and *Rorc*$^{-/-}$ (Th17 cells^{-}ILC3s^{+}) mice were injected into lethally irradiated recipients (Figure 4A). The depletion and reconstitution efficiency detected in these chimeric mice confirmed the successful modification of the intended models (Figures S4B–S4D). Compared to mice reconstituted with WT-BM (Th17 cells^{+}ILC3s^{+}), mice receiving *Rag1*$^{-/-}$ and *Rorc*$^{-/-}$ mix-BM (Th17 cells^{-}ILC3s^{+}) exhibited smaller fibrotic niches and reduced α-SMA intensity, evidence of a profibrotic role for Th17 cells. Mice reconstituted with *Rorc*$^{-/-}$-BM

(Th17 cells^{-}ILC3s^{-}) showed a further reduction in fibrotic niche size, in contrast to those reconstituted with mix-BM (Th17 cells^{-}ILC3s^{+}), illustrating an additional fibrogenic role for ILC3s (Figures 4B and 4C). Across all models, spatial organization and numbers of ILC3s within kidneys were positively associated with fibrotic niche sizes (Figure 4D).

The non-redundant contribution of ILC3s in the presence of Th17 cells was further supported by adoptively transferring T cells with or without ILC3s into *Rorc*$^{-/-}$-UUO mice (Figure 4E). In this case, compared to mice receiving T cells plus ILC3s, *Rorc*$^{-/-}$-UUO receiving T cells lacked only ILC3s (Figure S4E) and displayed smaller fibrotic niche size and less ECM deposition (Figures 4F and 4G), demonstrating the non-redundancy of ILC3s during renal fibrosis.

In a more physiological context, we treated *Rag1*$^{-/-}$-UUO mice with anti-CD90.2 monoclonal antibody to deplete ILC3s *in vivo* (Figures 4H and S4F),[44] and identified a smaller fibrogenic niches size, attenuation of ECM production in UUO kidney post-ILC3s depletion (Figures 4I and 4J). Conversely, adoptive transfer of sorted SI-ILC3s drastically increased ILC3s in the kidney (Figures 4K and S4G–S4I) and exacerbated fibrosis in *Rag1*$^{-/-}$-UUO kidneys (Figures 4L and 4M), confirming the pro-fibrotic efficiency of intestinal ILC3s even in the absence of adaptive lymphocytes.

Elevated PD-1 expression enhanced the pro-fibrotic role of kidney-infiltrating ILC3s

Immune checkpoints are critical in modulating immune activity by stimulating or inhibiting signals in immune cells, including ILCs.[45–49] To define how immune checkpoints change in these migratory ILC3s and whether they are relevant in fibrotic kidneys, we mapped immune checkpoint-related genes in renal and intestinal ILC3s based on scRNA-seq data. *Pdcd1*, encoding PD-1, was increased in fibrotic kidney-infiltrating ILC3s appeared as compared to intestinal ILC3s, especially as fibrosis progressed (Figure 5A). When visualizing *Cxcr6* transcript expression in the fibrotic kidney, *Pdcd1*$^{+}$ ILC3s exhibited a significant co-expression of *Cxcr6* (Figure 5B), which was confirmed at the protein level by flow cytometry (Figure 5C). This suggests it is the newly migrated CXCR6^{+} ILC3s that expressed PD-1 in the fibrotic kidney. In addition, the proportion and expression intensity of PD-1 on renal ILC3s in both UUO and FAN kidneys gradually increased during fibrogenesis (Figures 5D and 5E). Conversely, ILC3s in the intestines and peripheral blood exhibited minimal PD-1 expression (Figures S5A–S5C).

PD-1^{+} ILC3s will reside in human decidua and tumor tissues,[50–52] with impaired cytokine production and responses against tumors. In kidney sections from patients with CKD, PD-1^{+} ILC3s were localized to fibrotic structures expressing α-SMA (Figure S5D). A similar pattern was found in mice kidneys (Figure S5E). Moreover, in areas with more severe fibrosis, we observed an enrichment of PD-1^{+}CD127^{+} ILCs, but not PD-1^{-}CD127^{+} ILCs (Figures 5F and 5G), indicating PD-1^{+} ILC3s likely exert pro-fibrotic functions. To probe this further, we utilized *Pdcd1*$^{-/-}$ mice. First, PD-1 deficiency did not affect the plasticity and development of intestinal ILC3s (Figure S5F), the expression of CXCR6 thereon (Figure S5G), or the numbers of kidney- and SI-ILC3s (Figure S5H), indicating that loss of PD-1 did not impair ILC3s mobility. We next examined whether PD-1 mediates the pro-fibrotic effects of ILC3s by adoptively transferring purified SI-ILC3s from *Pdcd1*$^{-/-}$ or WT mice

into UUO recipients (Figure 5H). Mice receiving *Pdcd1*$^{-/-}$-ILC3s had fewer α-SMA^{+} activated myofibroblasts and lower expression of fibrogenic markers in the kidneys when compared to those received WT-ILC3s (Figures 5I and 5J). These data demonstrate that PD-1 expression on ILC3s exacerbates renal fibrosis.

PD-1 on ILC3s increases IL-17A production to enhance fibroblasts activation

To gain mechanistic insight into the effects of PD-1^{+} ILC3s on kidney fibrosis, CD45^{+}LIN^{-}CD127^{+} ILCs were isolated from *Pdcd1*$^{-/-}$-UUO3d kidneys for scRNA-seq. Compared with WT-ILC3s, 143 genes were decreased and 190 genes were increased in *Pdcd1*$^{-/-}$-ILC3s (Figure 6A). Among the main effector cytokines of ILC3s, *Il17a* was decreased by PD-1 deletion (Figure 6B). Subsequent analysis confirmed that, unlike ILC3s in intestine that produce negligible IL-17A (Figure S6A), kidney ILC3s from UUO mice and CKD patients generate considerable IL-17A (Figures 6C, 6D; Table S4). Moreover, PD-1^{+} ILC3s in fibrotic kidneys were capable of increased IL-17A secretion than *Pdcd1*$^{-/-}$-ILC3s, which produced minimal IL-17A (Figure 6D).

To assess whether ILC3s promote renal fibrosis via PD-1-mediated IL-17A secretion, we generated *Pdcd1* conditional deletion mice (Figure 6E). *Rorc-cre* mice were crossed with *Pdcd1-flox* mice to obtain *Pdcd1*$^{fl/fl}$*Rorc-cre* mice that specifically deleted PD-1 on RORγt^{+} cells, and *Pdcd1*$^{fl/fl}$ mice were set as controls (Figures 6F, S6B, and S6C). Since Th17 cells, the counterpart of ILC3s, are considered important sources of IL-17A,[22] and *Pdcd1*$^{fl/fl}$*Rorc-cre* mice lack PD-1 on ILC3s and Th17 cells, we simultaneously examined how loss of PD-1 affected IL-17A secretion by both in this model. We found that IL-17A production was reduced in ILC3s, but not Th17 cells, in *Pdcd1*$^{fl/fl}$*Rorc-cre*-UUO mice compared to controls (Figure 6G and S6D), demonstrating ILC3-specific regulation of IL-17A by PD-1 within the fibrotic renal environment. *Pdcd1*$^{fl/fl}$*Rorc-cre*-UUO mice also displayed diminished renal fibrosis than *Pdcd1*$^{fl/fl}$-UUO controls (Figure 6H), indicating that PD-1-mediated IL-17A production by ILC3s may accelerate renal fibrosis. We also observed a temporal disparity in the ability of Th17 cells and ILC3s to produce IL-17A. Specifically, ILC3s displayed a greater capacity for IL-17A production compared to Th17 cells at UUO6h and UUO1d (Figures S6E and S6F), which, combined with the time-sensitive infiltration of ILCs (Figure S2A), suggests their precedence in triggering fibrosis.

As important effectors of innate immunity, ILC3s orchestrate immune subsets to promote inflammation and disease development.[4,53] However, in our adoptive transfer experiments, T cells and macrophages were not affected by renal ILC3s (Figure S6G). Instead, ILC3s, particularly PD-1^{+} ILC3s, accumulated around α-SMA^{+} myofibroblasts within fibrotic structures, underscoring their ability to directly promote renal myofibroblast expansion. Further exploration in an angiotensin II-induced fibroblast activation model revealed that co-culture of ILC3s with primary mouse kidney fibroblasts elevated fibrotic genes expression and ECM production, a process also triggered by purified rmIL-17A (Figures 6I–6K). However, co-culturing with *Pdcd1*$^{-/-}$-ILC3s failed to increase fibrosis markers, which was comparable to the effect of WT-ILC3s pretreated with neutralizing anti-IL-17A antibodies (Figures 6J and 6K). These findings collectively suggest that PD-1^{+} ILC3s render pro-fibrotic effects primarily by activating fibroblasts through IL-17A production.

PD-1 amplifies IL-23-induced JAK2/STAT3/RORγt/IL-17A signaling in ILC3s by competitively binding to IL-23R to inhibit endocytosis

In UUO kidneys, RORγt expression was reduced in *Pdcd1*$^{-/-}$-ILC3s compared to WT-ILC3s (Figure 7A). Further analysis confirmed that this reduction did not result from ILC3s transitioning to ILC1s or ILC2s in the absence of PD-1 but rather described a distinct functional subtype of ILC3s (Figure S7A).

Given that STAT3 directly regulates RORγt,[54,55] we examined phospho-STAT3 (p-STAT3) levels in purified SI-ILC3s upon stimulation of IL-23/IL-1β, two cytokines essential for ILC3 activation. IL-23/IL-1β were confirmed to be elevated in UUO kidneys and induced PD-1 expression in SI-ILC3s (Figures S7B and S7C). While WT-ILC3s showed increased p-STAT3 after stimulation, *Pdcd1*$^{-/-}$-ILC3s exhibited resistance (Figure 7B). Meanwhile, chemical block of p-STAT3 with small-molecule inhibitor (Stattic) reduced IL-23/IL-1β-induced IL-17A production and RORγt expression in WT-ILC3s (Figures 7C, 7D, and S7D). These data support that PD-1 regulates ILC3 activity through a STAT3/RORγt pathway.

The next question was how does PD-1 connect to STAT3 activation. Starting from surface receptors IL-1R1 and IL-23R, we screened proteins upstream of STAT3. IL-1R1 was not significantly expressed on SI-ILC3s before and after stimulation (Figure S7E). In contrast, SI-ILC3s expressed abundant IL-23R at steady state, which was enhanced by IL-23/IL-1β stimulation. However, this increase was abolished when ILC3s lacked PD-1 (Figure 7E). In line, immunostaining showed that phospho-JAK2 (p-JAK2), a signal between IL-23R and STAT3, was also not elevated in *Pdcd1*$^{-/-}$-ILC3s after stimulation as in WT-ILC3s (Figure 7F). These results implicated IL-23R as the main receptor and we proposed that PD-1 may directly regulate the IL-23R.

IL-23R signaling is essentially determined by its surface expression, which is regulated by IL-23 induction.[56,57] Intracellular staining for IL-23R expression by flow cytometry revealed comparable total IL-23R expression between WT-ILC3s and *Pdcd1*$^{-/-}$-ILC3s (Figure 7G). The reduced surface IL-23R and unchanged total IL-23R levels in *Pdcd1*$^{-/-}$-ILC3s compared to WT-ILC3s suggested that PD-1 does not affect overall IL-23R expression but modulates its cellular translocation. After IL-23 stimulation, surface IL-23R undergoes clathrin-mediated endocytosis (CME) and endosomal recycling, which has been reported in macrophages and T cells.[58,59] Consequently, we hypothesized that PD-1 may suppress IL-23R endocytosis to preserve IL-23/STAT3 signaling. Further chlorpromazine (CPZ, a CME inhibitor) treatment showed no obvious effect on WT-ILC3s, but restored the reduction of surface IL-23R, cellular RORγt, and IL-17A in *Pdcd1*$^{-/-}$-ILC3s, reaching levels equivalent to WT-ILC3s (Figures 7H–7J).

To delve deeper into the molecular interactions, we then turned to AlphaFold2 for structural predictions of PD-1 and IL-23R. The data suggested a high probability of hydrophobic interactions between the two proteins (Figure 7K), and co-immunoprecipitation (Co-IP) confirmed the presence of protein binding (Figure 7L). Initiation of CME is triggered by recruitment of adapter protein 2 (AP2) to the receptor.[60] Further AlphaFold2 analysis revealed an overlap between PD-1-IL-23R binding and AP2-IL-23R binding (Figure S7F),

that is, PD-1 may inhibit AP2 recruitment to IL-23R, thereby blocking endocytosis. Subsequent Co-IP confirmed that AP2 binding to IL-23R was significantly reduced in the presence of PD-1 (Figure 7M).

Altogether, these results demonstrated that PD-1 may impede IL-23R endocytosis by competitively binding to it, thus ensuring greater IL-23R availability for IL-23 stimulation on the ILC3s plasma membrane, thereby amplifying downstream JAK2/STAT3/RORγt/IL-17A signaling of ILC3s to promote fibroblast activation and renal fibrogenesis (Figure 7N).

DISCUSSION

ILC3s play pivotal roles in tissue immunity and homeostasis, but their roles in renal fibrosis are unknown. Peripheral blood ILC subsets in CKD patients undergo significant changes and correlate with kidney function and disease activity, suggesting ILCs are associated with renal fibrosis progression.[61] However, the effects on ILCs in kidney tissues are less clear. Here, we revealed an ILC accumulation within fibrotic kidneys, positively associating with the extent of fibrosis, and ILC3s dominated ILC subsets in the circulation and kidney of both CKD patients and murine models of renal fibrosis. Further experiments revealed that, in response to kidney injuries, intestinal ILC3s were mobilized and migrated to the kidney quickly via the CXCR6/CXCL16 axis. These ILC3s enhanced PD-1 expression in the renal fibrotic microenvironment and potentiated renal fibrogenesis in a PD-1-dependent manner. Mechanistically, PD-1 augmented STAT3/RORγt-dependent IL-17A production via regulating IL-23R endocytosis in ILC3s, directly triggering fibroblast activation and fibrotic niche formation. Similarly, ILC3s promote hepatic stellate cell fibrogenesis via IL-17A/IL-22, exacerbating liver fibrosis.[6] These data support that ILC3s/IL-17A axis may be the common denominator for various tissue fibrosis.

Despite being recognized as a minority in kidney, ILCs play critical roles in renal fibrosis, reiterating that cell numerical superiority does not directly correlate with transcendent effects on disease. Emerging studies have focused on the involvement of relatively rare immune cells in kidney disease, such as basophils, γδ T cells, and mucosal-associated invariant T cells (MAITs).[62–66] These cells secrete an early wave of cytokines and trigger subsequent inflammation, playing an indispensable role in disease occurrence and progression. Therefore, it is advantageous to focus on these untapped tiny but mighty bodies.

IL-17A is profibrotic in renal fibrosis, with Th17 cells suggested as major sources.[22] Our BMT experiments provided direct evidence for the role of Th17 cells through an intercomparison strategy of Th17 cells and ILC3s. Focusing on ILC3s, we identified that ILC3s were an important contributor to renal IL-17A with non-redundant fibrogenesis roles beyond Th17 cells. Although both cells were important sources of IL-17A in renal fibrosis, the impact of PD-1 on IL-17A production differs between ILC3s and Th17 cells. This was a finding in *Pdcd1*$^{fl/fl}$*Rorc-cre*-UUO mice, where PD-1 deletion attenuated IL-17A in ILC3s but not in Th17 cells. These findings underscore the distinct roles of PD-1 in different cells and reinforce that PD-1-mediated IL-17A production in ILC3s is crucial for renal fibrosis. Therefore, although ILC3s and Th17 cells produced the same cytokine IL-17A, the distinct

PD-1 mediated activation mechanisms, combined with the unique characteristics of ILC3s – such as their derivation from a substantial gut reservoir, rapid accumulation, and IL-17A secretion in the kidneys, and preferential localization within fibrotic regions – endow ILC3s with their independent and unique role in exerting profibrotic effects in comparison to Th17 cells.

PD-1 was initially discovered on T cells and is thought to recruit phosphatases (e.g., SHP-2) to its immunoreceptor tyrosine switch motif (ITSM), thereby initiating dephosphorylation of the T cell receptor (TCR) signaling and inactivation.[67] PD-1 is also expressed on ILC subsets.[46–48] However, due to the lack of TCR, the inhibitory effect of PD-1 on immune synapse formation is assumed to be greatly weakened on ILCs. Then PD-1 may regulate ILCs' function in other ways. Here, we uncovered that PD-1 functions to amplify IL-23-induced JAK2/STAT3/RORγt/IL-17A signaling in ILC3s. Specifically, PD-1 directly binds to IL-23R and competitively occupies the binding site of AP2, thus inhibiting the endocytosis of IL-23R initiated by AP2 to maintain its surface expression and achieve final downstream activation. By the same token, PD-1 might also bind to other receptors and affect their endocytosis, regulating other immune cells. These conjectures may bring versatility to the future prospects of PD-1 intervention. Our study provides insights into PD-1-mediated immune regulation and establishes a foundation for PD-1- and IL-23/STAT3/IL-17A pathway-targeted therapies in renal fibrosis.

The origin and migration of ILC3s in non-barrier tissue is not well understood. ILC2s can undergo SI-lung or lung-liver migration during inflammation.[68,69] In line, our data show that post-kidney injury, ILC3s are mobilized from their abundant intestinal pool under the regulation of CXCR6/CXCL16 axis. Collectively, these findings underscore the capability of ILCs for inter-organ migration to provide immune effects in distant sites; in our context, further emphasizing the "gut-renal axis" immune pathway. Since this theory was proposed, the role of intestinal immunity in kidney disease has garnered increasing interest.[70–72] Patients with IgA nephropathy (IgAN), one of the leading causes of CKD, treated with the intestinal mucosal immune-targeted release formulation of glucocorticoid budesonide can achieve striking recoveries with a favorable safety pattern.[73] This agent has been approved by the FDA to treat IgAN, further highlighting the clinical translation value of gut-kidney interaction. However, underlying mechanisms involved in gut-kidney dialogue remain unclear. Our finding provided evidence for the immune mechanisms of the gut-kidney axial regulation, suggesting that blocking ILC3s gut-kidney trafficking might offer additional targeting opportunities in renal fibrosis. This study also indicates that the reduction of intestinal ILC3s that occurs in the progression of CKD may be partly responsible for the gastrointestinal disturbances in patients, as a normal level of ILC3s is essential for maintaining intestinal homeostasis. Thus, blocking ILC3 migration may also help alleviate CKD-associated gastrointestinal dysfunction. Furthermore, in the current study, we observed intestinal ILC3s trafficked to other organs in small amounts post-kidney injury, suggesting that ILC3s may participate in multi-organ dysfunction in CKD. The mechanisms by which they migrate to these sites and what role they play merit future exploration.

Limitations of the study

While the models of UUO and FAN are widely accepted and extensively utilized in the field of renal fibrosis research, as they recapitulate the fundamental pathogenetic processes of CKD, they cannot perfectly encapsulate the complete spectrum of all forms of human CKD. Our study demonstrated a significant decrease of SI-ILC3s in murine models, but ethical constraints on obtaining intestine specimens in CKD patients prevented us from further verification in humans. In addition, ILC3s could drive renal fibrogenesis by directly activating fibroblasts, but might also establish a profibrotic environment by interacting with other immune or renal cells *in vivo* as well, warranting comprehensive scRNA-seq analyses to decipher these interactions. However, further cell-cell interaction analysis might be limited by insufficient available renal ILC3s. Finally, other immune cells in SI were detected to undergo gut-kidney migration during kidney injury, but how these cells participate in renal fibrosis remains to be thoroughly studied in the future.

STAR METHODS

RESOURCE AVAILABILITY

Lead contact—Information and requests for resources and reagents should be directed to and will be fulfilled by the lead contact, Yi Zhou (zhouyi39@mail.sysu.edu.cn).

Materials availability—Further information and requests for resources and reagents should be directed to and will be fulfilled by the lead contact. This study did not generate new unique reagents.

Data and code availability

- Raw and processed scRNA-seq data have been deposited to GEO: GSE249724.
- This paper does not report original code.
- Any additional information required to reanalyze the data reported in this paper is available from the lead contact upon reasonable request.

EXPERIMENTAL MODEL AND STUDY PARTICIPANT DETAILS

Animals—Wild type mice (CD45.2) were purchased from Beijing Vital River Laboratory Animal Technology Co., Ltd. *Pdcd1*$^{-/-}$ mice (JAX #028276), *Rag1*$^{-/-}$ mice (JAX #002216), *Rorc*$^{-/-}$ mice (JAX #007571), *Rorc-cre* mice (JAX #022791), *Cxcr6*$^{gfp/gfp}$ mice (JAX #005693), and CD45.1 mice (JAX #002014) were purchased from The Jackson Laboratory (Bar Harbor, Maine, USA). *Pdcd1*$^{fl/fl}$ mice (Cat. NO. NM-CKO-210063) were obtained from Shanghai Model Organisms Center, Inc. *Kaede* transgenic mice were purchased from the RIKEN BioResource Center (Tsukuba, Ibaraki, Japan). Mice were bred and maintained in the laboratory animal center of Sun Yat-Sen University in specific pathogen-free (SPF) facilities at room temperature, and were given the same and regular diet. Less than 5 mice were co-housed within each cage. All mice were of C57BL/6 background, and 8–10-week-old male mice were used for all experiments. All mice study was performed in accordance with the protocol approved by the Animal Care and Use Committee of the Sun Yat-Sen University.

Cell lines and primary cell cultures—HEK-293T (ATCC, CRL-3216) was cultured with DMEM medium, supplemented with 10% fetal bovine serum (FBS) and 1% Penicillin/ Streptomycin.

Primary renal fibroblasts were isolated from UUO mice. Cells were grown in DMEM/F12 medium, supplemented with 10% FBS and 1% Penicillin/ Streptomycin.

Primary intestinal ILC3s were isolated from the mice small intestines by flow cytometry. Cells were cultured with RPMI 1640 medium, supplemented with 10% FBS and 1% Penicillin/Streptomycin.

All the cells were cultured at 37°C in 5% CO_2.

Patients and specimens—Kidney tissues or sections in this study were derived from kidney biopsies from CKD patients or normal kidney tissues from patients with renal carcinoma. Peripheral blood samples were derived from CKD patients or healthy donors. CKD patients were classified into non-fibrosis group and fibrosis group according to histological lesions, and those with urinary tract infections or renal tumors were excluded. The demographic and clinical characteristics of the patient cohorts are listed in Tables S1–S4. Samples were obtained from the Department of Nephrology, The First Affiliated Hospital of Sun Yat-sen University. All participants provided informed consent and this study was approved by the Ethical Committee of the First Affiliated Hospital of Sun Yat-Sen University (Approval no. 2022(602), 2016(215)).

METHOD DETAILS

Animal experiments—UUO renal fibrosis models were performed as previously described[74]. Briefly, groups of male mice were anesthetized by intraperitoneal injection of 0.5% sodium pentobarbital, and the left ureter was ligated twice with silk sutures before being cut. The mice were kept at a constant body temperature of 37 °C. Sham-operated mice had their ureters exposed and manipulated without ligation.

FA-induced renal fibrosis models were performed by a single dose of intraperitoneal injection with folic acid (300mg/kg, Sigma-Aldrich), which dissolved in the vehicle of $NaHCO_3$ (25.2g/L, Macklin). Control mice received the same dose vehicle.

For IRI-induced renal fibrosis models, mice were anesthetized by intraperitoneal injection of 0.5% sodium pentobarbital. Then the abdominal skin was cut open, both kidneys were exposed and the renal pedicles were clamped for 30 min. The mice were kept at a constant body temperature of 37 °C. In the sham-operated mice, only anesthesia and muscle incision were performed.

For photoconversion of *Kaede* transgenic mice, after the surrounding tissue was covered with aluminum foil, the small intestines were exposed to violet light at 95 mW/cm^2 with a 436-nm bandpass filter using Spot UV curing equipment (SP9; USHIO).

Genotyping of transgenic mice—The Phire Tissue Direct PCR Master Mix Kit (Thermo) was used for DNA isolation and subsequent PCR. According to the

manufacturer's instructions, mice toe samples were dissolved in 20 μl Dilution Buffer supplemented with 0.5 μl DNA Release Additive for 1 h at 98°C. 1 μl supernatant was used for PCR reaction using 2x Phire Tissue Direct PCR Master Mix. PCR products were separated on a 1.5% agarose gel and visualized with ethidium bromide. Primers used are listed in Table S5.

Multiplex immunofluorescence staining of patient kidney sections—Multiplex immunofluorescence [75] was performed using a PANO 7-plex IHC kit (Panovue, Beijing, China). After different primary antibodies were applied sequentially, horseradish peroxidase-conjugated secondary antibody incubation and tyramide signal amplification (TSA) were performed. The slides were microwave heat-treated after each TSA operation. Nuclei were stained with 4′,6-Diamidino-2-phenylindole dihydrochloride (DAPI) after all the antigens had been labelled. Then the stained slides were scanned using the PanoVIEW vs200 slide scanner (Panovue, Beijing, China) to obtain multispectral images. Fluorescence spectra were captured at 460nm, 480nm, 520nm, 570nm, 650nm, 780nm with identical exposure time. Multispectral images were analyzed, including MFI of each marker and cell quantification at single-cell level, with QuPath v0.2.0 image analysis software (Queen's University Belfast, Northern Ireland, UK) on a PanoATLAS workstation. According to α-SMA expression level, the slides were divided into fibrotic areas and non-fibrotic areas, and the $CD3^{-}ROR\gamma t^{+}$ ILC3s in different areas were compared.

Isolate leukocytes from kidneys, small intestines, lungs, spleens, lymph nodes and peripheral blood.—For human kidney samples, fresh tissues were cut into approximately 1 mm^3 pieces and digested using the Multi Tissue dissociation kit (Miltenyi Biotec). According to the manufacturer's instructions for the kit, up to 0.25 g of the mincing tissue was mixed with 100 μl of Enzyme D, 50μl of Enzyme R and 12.5 μl of Enzyme A in 2.35 ml of RPMI 1640. The mixture was then transferred into gentleMACS C Tubes (Miltenyi Biotec) and incubated for 1 h at 37°C with gentleMACS Octo Dissociator (Miltenyi). Following digestion, the solution was passed through 70 μm cell strainers, centrifuged, and suspended with PBS.

For mice kidneys, tissues were harvested after perfusion with cold PBS and minced in cold RPMI 1640 containing 2%FBS, then were digested in a 10 ml digestion medium (RPMI 1640, 2%FBS, 1mg/ml Collagenase type II, 0.5mg/ml Dispase; all Gibco) for 30 min at 37 °C, and stirred at 180–200 rpm. The tissues were neutralized with PBS, then filtered (70 μm), centrifuged, and resuspended in PBS with 1%FBS.

Small intestines were harvested and the contents were emptied with cold PBS. The fat and Peyer's patches were removed before the intestines were turned inside out and cut into small pieces. The tissues then were incubated in 25 ml extraction medium (RPMI 1640, 2%FBS, 5mM DTT, 1mM EDTA) for 15 min at 37 °C, stirred at 180–200 rpm to dissociate intraepithelial leukocytes. The remained fragments were washed with PBS, and then digested in 25 ml digestion medium (RPMI 1640, 2%FBS, 1mg/ml Collagenase type II, 0.5mg/ml Dispase; all Gibco). The tissues were neutralized with PBS, then filtered (70 μm), centrifuged, and resuspended in PBS with 1%FBS.

Lung tissues were harvested after perfusion and were disrupted into small pieces, then were digested in 10 ml digestion medium (RPMI 1640, 2%FBS, 1mg/ml Collagenase type I, 0.5mg/ml Dispase; all Gibco) for 30 min at 37 °C, stir at 180–200 rpm. The tissues were neutralized with PBS, then filtered (70 μm), centrifuged, and resuspended in PBS with 1%FBS.

Spleens, lymph nodes were ground on the cell strainer (70 μm) with a syringe plunger, and then centrifuged. Red blood lysis was performed where was necessary. Then, the tissues were neutralized with PBS, centrifuged, and resuspended in PBS with 1%FBS.

Bone marrow cells were collected by flushing femurs and tibiae with RPMI 1640 containing 2% FBS. Then red blood lysis was performed.

PBMC of humans or mice were isolated from whole blood with Ficoll (GE Healthcare) according to the manufacturer's instructions.

Flow cytometry and cell sorting.—Subsequent to getting the single cell suspension from different tissues, cells were incubated with surface staining flow cytometry antibodies for 30 min at 4°C in the dark. The cells were then treated with the fixation/permeabilization kit (eBioscience). Succeeding washing, cells were stained with intracellular antibodies for 45 min to 1 h at room temperature (RT) in the dark. For intracellular cytokine staining (IL-17A), the cells were stimulated with a cell stimulation cocktail (including PMA and ionomycin plus protein transport inhibitors, eBioscience) for 4–6 h. Cells were analyzed on Attune NxT flow cytometer (Thermo Fisher Scientific) and data were analyzed with FlowJo software. For cell sorting, cells were stained with surface staining flow cytometry antibodies for 30 min at 4 °C in the dark, then purified on BD Influx cell sorter (BD Biosciences). ILCs were identified as $CD45^+Lin^-CD127^+$; ILC3s were identified as $CD45^+Lin^-CD127^+CD117^+$. Detailed information regarding antibodies is listed in the key resources table.

Single-cell RNA Sequencing experiment—Intestinal ILC3s and renal ILCs were sorted by flow cytometry. Intestinal ILC3s from three mice per group were pooled together for further scRNA-seq; renal ILCs from ten mice per group were pooled together for further scRNA-seq. BD Rhapsody system was used to capture the transcriptomic information of the renal ILCs single cells. Single-cell capture was achieved by random distribution of a single-cell suspension across > 200,000 microwells through a limited dilution approach. Beads with oligonucleotide barcodes were added to saturation so that a bead was paired with a cell in a microwell. The cells were lysed in the microwell to hybridize mRNA molecules to barcoded capture oligos on the beads. Beads were collected into a single tube for reverse transcription and ExoI digestion. Upon cDNA synthesis, each cDNA molecule was tagged on the 5′ end (that is, the 3′ end of a mRNA transcript) with a unique molecular identifier (UMI) and cell barcode indicating its cell of origin. Whole transcriptome libraries were prepared using the BD Rhapsody single-cell whole-transcriptome amplification (WTA) workflow including random priming and extension (RPE), RPE amplification PCR and WTA index PCR. The libraries were quantified using a High Sensitivity DNA chip (Agilent) on a Bioanalyzer

2200 and the Qubit High Sensitivity DNA assay (Thermo Fisher Scientific). Sequencing was performed by illumina sequencer (Illumina, San Diego, CA) on a 150 bp paired-end run.

Single-cell RNA Statistical Analysis—Single-cell RNA-seq data analysis was performed by NovelBio Bio-Pharm Technology Co., Ltd. with NovelBrain Cloud Analysis Platform. We applied fastp[76] with default parameter filtering the adaptor sequence and removed the low-quality reads to achieve the clean data. UMI-tools[77] were applied for Single Cell Transcriptome Analysis to identify the cell barcode whitelist. The UMI-based clean data was mapped to mouse genome (Ensemble version 100) utilizing STAR[78] mapping with customized parameter from UMI-tools standard pipeline to obtain the UMIs counts of each sample. Cells contained over 200 expressed genes and mitochondria UMI rate below 20% passed the cell quality filtering and mitochondria genes were removed in the expression table. After excluding low-quality cells and contaminating lineage cells, we finally obtained 8,294 renal ILC cells (WT-UUO3d: 3,362 cells, WT-UUO14d: 2,640 cells, PD-1 KO-UUO3d: 2,292 cells), and 7,288 intestinal ILC3 cells (WT-UUO0d: 3,128 cells, WT-UUO3d: 4,160 cells). Seurat package (version: 3.1.4, https://satijalab.org/seurat/) was used for cell normalization and regression based on the expression table according to the UMI counts of each sample and percent of mitochondria rate to obtain the scaled data. PCA was constructed based on the scaled data with the top 2,000 high variable genes and top 10 principals were used for UMAP construction.

Utilizing graph-based cluster method (resolution = 0.8), we acquired the unsupervised cell cluster result based on the PCA top 10 principal and we calculated the marker genes by FindAllMarkers function with wilcox rank sum test algorithm under following criteria:1. lnFC > 0.25; 2. pvalue<0.05; 3. min.pct>0.1. In order to identify the cell type in detail, the clusters of same cell type were selected for UMAP analysis, graph-based clustering and marker analysis. Differentially expressed genes identified by DESeq2 (fold change > 1.2, $P < 0.05$) were highlighted in the volcano plot. Pathway analysis was used to find out the significant pathway of the differential genes according to KEGG database. We turn to the Fisher's exact test to select the significant pathway, and the threshold of significance was defined by P-value and FDR. We applied the Single-Cell Trajectories analysis utilizing Monocle2 (http://cole-trapnell-lab.github.io/monocle-release) using DDR-Tree and default parameter. Before Monocle analysis, we select marker genes of the Seurat clustering result and raw expression counts of the cell passed filtering.

Immunofluorescence—For paraffin-embedded slides, tissues were fixed with 10% formalin overnight, and embedded with paraffin, then cut into 5-μm-thick sections. Then the slides were processed to remove paraffin and then hydrated in alcohol and phosphate-buffered saline. The slides were made permeable in 0.2% Triton X-100 (Sigma-Aldrich) and then blocked with 10% normal donkey serum (Sigma-Aldrich) followed by incubated with primary antibodies overnight at 4 °C. After staining primary antibodies, slides were stained with corresponding fluorescence-labeled secondary antibodies for 1 h at room temperature. Nuclei were stained with DAPI.

For snap-frozen slides, tissues were fixed in 4% paraformaldehyde overnight followed by dehydration in 30% sucrose for 4 h twice at 4 °C. Kidneys were then embedded in

OCT freezing media and stored at −80 °C. Tissues were cut into 5-μm-thick sections, and placed onto glass slides and stored at −80 °C until staining. Frozen sections were made permeable in 0.2% Triton X-100 (Sigma-Aldrich) and then blocked with 10% normal donkey serum (Sigma-Aldrich) followed by staining with antibodies diluted in blocking buffer overnight at 4 °C. After staining primary antibodies, slides were stained with corresponding fluorescence-labeled secondary antibodies for 1 h at room temperature. Nuclei were stained with DAPI. For small intestines and kidneys of *Kaede* mice, slides were incubated with DRAQ5 to label nuclei.

For cultured ILC3s, cells were centrifuged, suspended with PBS, and added to the polylysine-treated glass sides. Allow the slides to dry at 37 °C for 5–8 min, then cold methanol was dropwise on the slide for 20 min to fix the cells. Then the slides were made permeable and blockage with 0.2% Triton X-100 (Sigma-Aldrich) plus 10% normal donkey serum (Sigma-Aldrich) for 1 h at room temperature, followed by incubated with primary antibodies overnight at 4 °C. After staining primary antibodies, slides were stained with corresponding fluorescence-labeled secondary antibodies for 1 h at room temperature. Nuclei were stained with DAPI.

The slides were then mounted with Prolong Gold Antifade reagent (Invitrogen) and examined on a ZEISS LSM880 confocal microscope.

Detection of sCXCL16 in serum—The sCXCL16 in the serum of CKD patients or UUO mice were detected by commercial ELISA kits (SAB) according to the manufacturer's instructions. All samples were measured in duplicate.

In vivo CXCL16 neutralization—In order to block CXCL16 *in vivo*, mice received anti-CXCL16 neutralizing antibody (100μg/mouse each time, R&D Systems) intraperitoneally immediately, 1 day, and 2 days after UUO surgery. Whereas the control group received isotype antibody with the same dose. Mice were sacrificed for analysis 3 days after UUO surgery.

Antibody-mediated depletion of ILCs—For depleting the total ILCs in vivo, *Rag1*$^{-/-}$ mice were administered intraperitoneally with 3 doses of anti-CD90.2 antibody (250μg/mouse; BioXcell) or isotype control (250μg/mouse; BioXcell) every other day after UUO surgery[44]. The mice were sacrificed for analysis 3 days after UUO surgery.

Bone marrow transplantation—Bone marrow transplantation was conducted as described previously.[43] For detecting replacement efficiency, bone marrow cells (5×10^7) from CD45.1$^+$ mice were injected into CD45.2$^+$ recipient mice which were lethally irradiated with 5 Gy twice. For ILC3s depletion, bone marrow cells (5×10^7) from WT mice, *Rorc*$^{-/-}$ mice, or a mix of *Rorc*$^{-/-}$ and *Rag1*$^{-/-}$ mice (1:4) were transferred into WT recipient mice that were lethally irradiated with 5 Gy twice. After transplantation, the recipient mice were allowed to reconstitution for 8 w before UUO operation. The mice were sacrificed for analysis 3 or 7 days after UUO surgery.

Adoptive transfer experiments—Indicated single-cell suspensions of ILCs or ILC3s were sorted (purity > 93%) by flow cytometry. For adoptive transfer, 2–3×10^4 highly purified ILC3s or 2–2.5×10^5 T cells were injected intravenously into recipient mice 1 day after UUO. Mice were euthanized 3 days after UUO surgery.

RNA isolation and real-time PCR analysis—RNA was isolated from kidneys or harvested cells using RNeasy Mini kit (Qiagen) and then reverse transcribed into cDNA using Transcriptor First Strand cDNA Synthesis Kit (Roche) according to the manufacturer's instructions. Real-time PCR was run on the LightCycle 480 II (Roche) using SYBR Green PCR Master Mix and gene-specific primers. The data was normalized and analyzed using the delta CT or delta delta CT method. Primers used are listed in Table S6.

Western blot—Kidney cortex was lysed with RIPA buffer (Sigma-Aldrich) containing protease inhibitor cocktail (Roche). Lysates were centrifuged for 15 min at 4 °C, and the supernatants were obtained. Protein concentration was measured with the BCA protein assay. Samples were loaded and separated by 8–10% SDS polyacrylamide gels, electro-transferred onto a PVDF membrane, blotted with the indicated antibodies, and then detected by enhanced chemiluminescence (Amersham Pharmacia Biotech). GAPDH or α-tubulin was used as loading controls.

Cell Culture and treatment—For detecting PD-1 expression, RORγt expression and IL-17A production, purified SI-ILC3s were stimulated with IL-23 (10 ng/ml, R&D Systems) plus IL-1β (10 ng/ml, R&D Systems) for 48 h. For examining pSTAT3 expression, ILC3s were activated by IL-23 (20 ng/ml, R&D Systems) plus IL-1β (20 ng/ml, R&D Systems) for 20 min. For detecting IL-23R and IL-1R1 expression, ILC3s were activated by IL-23 (20 ng/ml, R&D Systems) plus IL-1β (20 ng/ml, R&D Systems) for 2 h; where indicated, ILC3s were pretreated with endocytosis inhibitor chlorpromazine (CPZ, 10μg/ml, Sigma-Aldrich) for 30 min before cytokine stimulation.

Primary renal fibroblasts were isolated and cultured as described previously[79]. For cytokine stimulation, fibroblasts were stimulated with mouse recombinant IL-17A (50 ng/ml, R&D Systems) for 24 h for further analysis. For co-culture with ILC3s, fibroblasts were quiesced by serum starvation and preincubated with Ang II (10^{-6} mol/L), then pre-activated ILC3s (1.5×10^4 cells in each well) were added at the cell ratio of 1:10 (ILC3s: fibroblasts) in the Trans-well co-culture systems (Corning) for 24 h. For IL-17A neutralization, the co-culture systems were added with neutralizing anti-IL-17A antibody (1μg/ml, R&D Systems). ILC3s were removed before collecting the fibroblasts for further analysis.

Structural prediction of PD-1-IL-23R complex with AlphaFold2—The structure of the PD-1-IL-23R complex was generated from the AlphaFold2[80] with the full-length protein sequences of PD-1 and IL-23R as input. Followed by the default setting with multimer mode, 5 AlphaFold2 initial models were produced and each model ran 5 interactions to output a total of 25 predicted models. Based on the template modeling and predicted alignment error values for each model, we picked out the top-ranked structure of the protein-protein complex with the most confident score as the final model of the subsequent analysis.

Co-immunoprecipitation (Co-IP) assay—60%–80% confluent 293T cells were co-transfected with pDNA3.1-Il23r (mouse)-3×FLAG or/and pcDNA3.1 (+)-Pdcd1 (mouse) (Hanyi, Guangzhou, China) using NEOFECT DNA transfection reagent (NEOFECT) for overexpressing IL-23R (3×FLAG-tagged) or/and PD-1. Cells were incubated with DMEM medium, supplemented with 10% FBS and 1% Penicillin/Streptomycin at 37 °C in 5% CO_2 for 48 h. Cells were harvested with NP-40 (Beyotime) supplemented with protease inhibitor and phosphatase inhibitor. Total protein lysate (2μg protein) was firstly incubated with protein A/G magnetic beads (MCE) at 4 °C for 4 h to preclear the lysate, then incubated with anti-flag antibody (2 μg, Proteintech), anti-PD-1 antibody (CST) or IgG (Proteintech) at 4 °C for 4 h. The protein-antibody complex was incubated with protein A/G magnetic beads at 4 °C overnight. Beads were collected and washed with PBST (PBS containing 0.05% Tween) three times. For immunoblotting, the beads were suspended with 1x loading buffer and boiled for 5 mins, and the supernatant was collected. The samples were separated on SDS-PAGE gel, transferred, blotted with anti-flag antibody, anti-PD-1 antibody, or anti-AP2 antibody and detected with horseradish peroxidase-conjugated anti-rabbit light-chain specific secondary antibody (Abbkine).

QUANTIFICATION AND STATISTICAL ANALYSIS

The details of the replicates for each experiment are listed in the respective figure legends. In brief, unless otherwise indicated, for most *in vitro* or *ex vivo* or *in vivo* studies, the data are pooled from or representative of two to four independent experiments and shown as mean ± SEM unless stated otherwise. Comparison among groups was assessed by Student's *t* test or one-way analysis of covariance (ANOVA), and correlations were analyzed with Pearson's correlation analysis. All statistical analysis was performed with the statistical software GraphPad Prism and p values < 0.05 were considered statistically significant. Statistical significance is defined as ****p < 0.0001, ***p < 0.001, **p < 0.01, *p < 0.05, or ns (not significant).

Supplementary Material

Refer to Web version on PubMed Central for supplementary material.

ACKNOWLEDGMENTS

This work was supported by the National Natural Science Foundation of China [82022009, 82270764 to Y.Z., 82370707, 82170737 to W.C.], the Guangdong Natural Science Fund [2017A030306013 to Y.Z.], Guangdong Special Support Program [2017TQ04R549 to Y.Z.], NHC Key Laboratory of Clinical Nephrology (Sun Yat-Sen University) and Guangdong Provincial Key Laboratory of Nephrology [2020B1212060028], the National Heart, Lung, and Blood Institute (HL151627, HL157073, and HL166538 to G.P.S.), and the National Institute of Neurological Disorders and Stroke (AG063839 to G.P.S). We thank NovelBioinformatics Co., Ltd. for technical expertise and guidance with bioinformatics analysis and their NovelBrain Cloud Analysis Platform (www.novelbrain.com); and Panovue Biotechnology (Beijing) Co., Ltd. for helping with human kidney ILC3s multiplex immunofluorescence staining and analysis; X. Li (Sun Yat-sen University Zhongshan School of Medicine) and S. Wang (BD Biosciences) for helping with the flow cytometry and cell sorting. We are grateful to X. Xia, W. Yang, Z. Lian, Y. Zhou and J. Zhou for their comments on the manuscript and helpful discussions.

REFERENCES

1. Vivier E, Artis D, Colonna M, Diefenbach A, Di Santo JP, Eberl G, Koyasu S, Locksley RM, McKenzie ANJ, Mebius RE, et al. (2018). Innate Lymphoid Cells: 10 Years On. Cell 174, 1054–1066. 10.1016/j.cell.2018.07.017. [PubMed: 30142344]
2. Bal SM, Golebski K, and Spits H (2020). Plasticity of innate lymphoid cell subsets. Nat Rev Immunol 20, 552–565. 10.1038/s41577-020-0282-9. [PubMed: 32107466]
3. Simoni Y, Fehlings M, Kloverpris HN, McGovern N, Koo SL, Loh CY, Lim S, Kurioka A, Fergusson JR, Tang CL, et al. (2017). Human Innate Lymphoid Cell Subsets Possess Tissue-Type Based Heterogeneity in Phenotype and Frequency. Immunity 46, 148–161. 10.1016/j.immuni.2016.11.005. [PubMed: 27986455]
4. Sonnenberg GF, and Hepworth MR (2019). Functional interactions between innate lymphoid cells and adaptive immunity. Nat Rev Immunol 19, 599–613. 10.1038/s41577-019-0194-8. [PubMed: 31350531]
5. Klose CS, and Artis D (2016). Innate lymphoid cells as regulators of immunity, inflammation and tissue homeostasis. Nat Immunol 17, 765–774. 10.1038/ni.3489. [PubMed: 27328006]
6. Wang S, Li J, Wu S, Cheng L, Shen Y, Ma W, She W, Yang C, Wang J, and Jiang W (2018). Type 3 innate lymphoid cell: a new player in liver fibrosis progression. Clin Sci (Lond) 132, 2565–2582. 10.1042/CS20180482. [PubMed: 30459204]
7. Grigg JB, Shanmugavadivu A, Regen T, Parkhurst CN, Ahmed A, Joseph AM, Mazzucco M, Gronke K, Diefenbach A, Eberl G, et al. (2021). Antigen-presenting innate lymphoid cells orchestrate neuroinflammation. Nature 600, 707–712. 10.1038/s41586-021-04136-4. [PubMed: 34853467]
8. Huang J, Fu L, Huang J, Zhao J, Zhang X, Wang W, Liu Y, Sun B, Qiu J, Hu X, et al. (2022). Group 3 Innate Lymphoid Cells Protect the Host from the Uropathogenic Escherichia coli Infection in the Bladder. Adv Sci (Weinh) 9, e2103303. 10.1002/advs.202103303. [PubMed: 35018740]
9. Hu C, Xu B, Wang X, Wan WH, Lu J, Kong D, Jin Y, You W, Sun H, Mu X, et al. (2023). Gut microbiota-derived short-chain fatty acids regulate group 3 innate lymphoid cells in HCC. Hepatology 77, 48–64. 10.1002/hep.32449. [PubMed: 35262957]
10. Raabe J, Kaiser KM, ToVinh M, Finnemann C, Lutz P, Hoffmeister C, Bischoff J, Goeser F, Kaczmarek DJ, Glowka TR, et al. (2023). Identification and characterization of a hepatic IL-13-producing ILC3-like population potentially involved in liver fibrosis. Hepatology 78, 787–802. 10.1097/HEP.0000000000000350. [PubMed: 37029085]
11. Melo-Gonzalez F, and Hepworth MR (2017). Functional and phenotypic heterogeneity of group 3 innate lymphoid cells. Immunology 150, 265–275. 10.1111/imm.12697. [PubMed: 27935637]
12. Goc J, Lv M, Bessman NJ, Flamar AL, Sahota S, Suzuki H, Teng F, Putzel GG, Bank JRILC, Eberl G, et al. (2021). Dysregulation of ILC3s unleashes progression and immunotherapy resistance in colon cancer. Cell 184, 5015–5030 e5016. 10.1016/j.cell.2021.07.029. [PubMed: 34407392]
13. Qiu J, Heller JJ, Guo X, Chen ZM, Fish K, Fu YX, and Zhou L (2012). The aryl hydrocarbon receptor regulates gut immunity through modulation of innate lymphoid cells. Immunity 36, 92–104. 10.1016/j.immuni.2011.11.011. [PubMed: 22177117]
14. Lo BC, Gold MJ, Hughes MR, Antignano F, Valdez Y, Zaph C, Harder KW, and McNagny KM (2016). The orphan nuclear receptor RORα and group 3 innate lymphoid cells drive fibrosis in a mouse model of Crohn's disease. Science Immunology 1. 10.1126/sciimmunol.aaf8864.
15. Bikbov B, Purcell CA, Levey AS, Smith M, Abdoli A, Abebe M, Adebayo OM, Afarideh M, Agarwal SK, Agudelo-Botero M, et al. (2020). Global, regional, and national burden of chronic kidney disease, 1990–2017: a systematic analysis for the Global Burden of Disease Study 2017. The Lancet 395, 709–733. 10.1016/s0140-6736(20)30045-3.
16. Romagnani P, Remuzzi G, Glassock R, Levin A, Jager KJ, Tonelli M, Massy Z, Wanner C, and Anders HJ (2017). Chronic kidney disease. Nat Rev Dis Primers 3, 17088. 10.1038/nrdp.2017.88. [PubMed: 29168475]
17. Distler JHW, Gyorfi AH, Ramanujam M, Whitfield ML, Konigshoff M, and Lafyatis R (2019). Shared and distinct mechanisms of fibrosis. Nat Rev Rheumatol 15, 705–730. 10.1038/s41584-019-0322-7. [PubMed: 31712723]

18. Huang E, Peng N, Xiao F, Hu D, Wang X, and Lu L (2020). The Roles of Immune Cells in the Pathogenesis of Fibrosis. Int J Mol Sci 21. 10.3390/ijms21155203.
19. Meng XM (2019). Inflammatory Mediators and Renal Fibrosis. Adv Exp Med Biol 1165, 381–406. 10.1007/978-981-13-8871-2_18. [PubMed: 31399975]
20. Tang PM, Nikolic-Paterson DJ, and Lan HY (2019). Macrophages: versatile players in renal inflammation and fibrosis. Nat Rev Nephrol 15, 144–158. 10.1038/s41581-019-0110-2. [PubMed: 30692665]
21. Humphreys BD (2018). Mechanisms of Renal Fibrosis. Annu Rev Physiol 80, 309–326. 10.1146/annurev-physiol-022516-034227. [PubMed: 29068765]
22. Peng X, Xiao Z, Zhang J, Li Y, Dong Y, and Du J (2015). IL-17A produced by both gammadelta T and Th17 cells promotes renal fibrosis via RANTES-mediated leukocyte infiltration after renal obstruction. J. Pathol. 235, 79–89. 10.1002/path.4430. [PubMed: 25158055]
23. Weng CH, Li YJ, Wu HH, Liu SH, Hsu HH, Chen YC, Yang CW, Chu PH, and Tian YC (2020). Interleukin-17A induces renal fibrosis through the ERK and Smad signaling pathways. Biomed Pharmacother 123, 109741. 10.1016/j.biopha.2019.109741. [PubMed: 31901549]
24. Chi HH, Hua KF, Lin YC, Chu CL, Hsieh CY, Hsu YJ, Ka SM, Tsai YL, Liu FC, and Chen A (2017). IL-36 Signaling Facilitates Activation of the NLRP3 Inflammasome and IL-23/IL-17 Axis in Renal Inflammation and Fibrosis. J Am Soc Nephrol 28, 2022–2037. 10.1681/ASN.2016080840. [PubMed: 28179433]
25. Artis D, and Spits H (2015). The biology of innate lymphoid cells. Nature 517, 293–301. 10.1038/nature14189. [PubMed: 25592534]
26. Ardain A, Domingo-Gonzalez R, Das S, Kazer SW, Howard NC, Singh A, Ahmed M, Nhamoyebonde S, Rangel-Moreno J, Ogongo P, et al. (2019). Group 3 innate lymphoid cells mediate early protective immunity against tuberculosis. Nature 570, 528–532. 10.1038/s41586-019-1276-2. [PubMed: 31168092]
27. Ryu S, Shin JW, Kwon S, Lee J, Kim YC, Bae YS, Bae YS, Kim DK, Kim YS, Yang SH, and Kim HY (2022). Siglec-F-expressing neutrophils are essential for creating a profibrotic microenvironment in renal fibrosis. J Clin Invest 132. 10.1172/JCI156876.
28. Chevalier RL, Forbes MS, and Thornhill BA (2009). Ureteral obstruction as a model of renal interstitial fibrosis and obstructive nephropathy. Kidney Int 75, 1145–1152. 10.1038/ki.2009.86. [PubMed: 19340094]
29. Norregaard R, Mutsaers HAM, Frokiaer J, and Kwon TH (2023). Obstructive nephropathy and molecular pathophysiology of renal interstitial fibrosis. Physiol Rev 103, 2827–2872. 10.1152/physrev.00027.2022. [PubMed: 37440209]
30. Eddy AA, Lopez-Guisa JM, Okamura DM, and Yamaguchi I (2012). Investigating mechanisms of chronic kidney disease in mouse models. Pediatr Nephrol 27, 1233–1247. 10.1007/s00467-011-1938-2. [PubMed: 21695449]
31. Fu Y, Tang C, Cai J, Chen G, Zhang D, and Dong Z (2018). Rodent models of AKI-CKD transition. American Journal of Physiology-Renal Physiology 315, F1098–F1106. 10.1152/ajprenal.00199.2018. [PubMed: 29949392]
32. Mackley EC, Houston S, Marriott CL, Halford EE, Lucas B, Cerovic V, Filbey KJ, Maizels RM, Hepworth MR, Sonnenberg GF, et al. (2015). CCR7-dependent trafficking of RORgamma(+) ILCs creates a unique microenvironment within mucosal draining lymph nodes. Nat Commun 6, 5862. 10.1038/ncomms6862. [PubMed: 25575242]
33. Kumar BV, Ma W, Miron M, Granot T, Guyer RS, Carpenter DJ, Senda T, Sun X, Ho SH, Lerner H, et al. (2017). Human Tissue-Resident Memory T Cells Are Defined by Core Transcriptional and Functional Signatures in Lymphoid and Mucosal Sites. Cell Rep 20, 2921–2934. 10.1016/j.celrep.2017.08.078. [PubMed: 28930685]
34. Turner JE, Becker M, Mittrucker HW, and Panzer U (2018). Tissue-Resident Lymphocytes in the Kidney. J Am Soc Nephrol 29, 389–399. 10.1681/ASN.2017060599. [PubMed: 29093030]
35. Tomura M, Yoshida N, Tanaka J, Karasawa S, Miwa Y, Miyawaki A, and Kanagawa O (2008). Monitoring cellular movement in vivo with photoconvertible fluorescence protein “Kaede” transgenic mice. Proc Natl Acad Sci U S A 105, 10871–10876. 10.1073/pnas.0802278105. [PubMed: 18663225]

36. Bjorklund AK, Forkel M, Picelli S, Konya V, Theorell J, Friberg D, Sandberg R, and Mjosberg J (2016). The heterogeneity of human CD127(+) innate lymphoid cells revealed by single-cell RNA sequencing. Nat Immunol 17, 451–460. 10.1038/ni.3368. [PubMed: 26878113]
37. Wang S, Qu Y, Xia P, Chen Y, Zhu X, Zhang J, Wang G, Tian Y, Ying J, and Fan Z (2020). Transdifferentiation of tumor infiltrating innate lymphoid cells during progression of colorectal cancer. Cell Res 30, 610–622. 10.1038/s41422-020-0312-y. [PubMed: 32367039]
38. Qiu X, Mao Q, Tang Y, Wang L, Chawla R, Pliner HA, and Trapnell C (2017). Reversed graph embedding resolves complex single-cell trajectories. Nat Methods 14, 979–982. 10.1038/nmeth.4402. [PubMed: 28825705]
39. Soriani A, Stabile H, Gismondi A, Santoni A, and Bernardini G (2018). Chemokine regulation of innate lymphoid cell tissue distribution and function. Cytokine Growth Factor Rev 42, 47–55. 10.1016/j.cytogfr.2018.02.003. [PubMed: 29472011]
40. Tian Y, Gong X, Qin D, Cao Y, Zhang S, Xia L, Liu F, and Su Z (2023). S1PR1-dependent migration of ILC3s from intestinal tissue to the heart in a mouse model of viral myocarditis. J Leukoc Biol 114, 154–163. 10.1093/jleuko/qiad048. [PubMed: 37141387]
41. Krebs CF, Paust HJ, Krohn S, Koyro T, Brix SR, Riedel JH, Bartsch P, Wiech T, Meyer-Schwesinger C, Huang J, et al. (2016). Autoimmune Renal Disease Is Exacerbated by S1P-Receptor-1-Dependent Intestinal Th17 Cell Migration to the Kidney. Immunity 45, 1078–1092. 10.1016/j.immuni.2016.10.020. [PubMed: 27851911]
42. Sanos SL, Bui VL, Mortha A, Oberle K, Heners C, Johner C, and Diefenbach A (2009). RORgammat and commensal microflora are required for the differentiation of mucosal interleukin 22-producing NKp46+ cells. Nat Immunol 10, 83–91. 10.1038/ni.1684. [PubMed: 19029903]
43. Magri G, Miyajima M, Bascones S, Mortha A, Puga I, Cassis L, Barra CM, Comerma L, Chudnovskiy A, Gentile M, et al. (2014). Innate lymphoid cells integrate stromal and immunological signals to enhance antibody production by splenic marginal zone B cells. Nat Immunol 15, 354–364. 10.1038/ni.2830. [PubMed: 24562309]
44. Dalli J, Colas RA, Arnardottir H, and Serhan CN (2017). Vagal Regulation of Group 3 Innate Lymphoid Cells and the Immunoresolvent PCTR1 Controls Infection Resolution. Immunity 46, 92–105. 10.1016/j.immuni.2016.12.009. [PubMed: 28065837]
45. Chiossone L, and Vivier E (2017). Immune checkpoints on innate lymphoid cells. J Exp Med 214, 1561–1563. 10.1084/jem.20170763. [PubMed: 28515074]
46. Helou DG, Shafiei-Jahani P, Lo R, Howard E, Hurrell BP, Galle-Treger L, Painter JD, Lewis G, Soroosh P, Sharpe AH, and Akbari O (2020). PD-1 pathway regulates ILC2 metabolism and PD-1 agonist treatment ameliorates airway hyperreactivity. Nat Commun 11, 3998. 10.1038/s41467-020-17813-1. [PubMed: 32778730]
47. Jacquelot N, Seillet C, Wang M, Pizzolla A, Liao Y, Hediyeh-Zadeh S, Grisaru-Tal S, Louis C, Huang Q, Schreuder J, et al. (2021). Blockade of the co-inhibitory molecule PD-1 unleashes ILC2-dependent antitumor immunity in melanoma. Nat Immunol 22, 851–864. 10.1038/s41590-021-00943-z. [PubMed: 34099918]
48. Taylor S, Huang Y, Mallett G, Stathopoulou C, Felizardo TC, Sun MA, Martin EL, Zhu N, Woodward EL, Elias MS, et al. (2017). PD-1 regulates KLRG1(+) group 2 innate lymphoid cells. J Exp Med 214, 1663–1678. 10.1084/jem.20161653. [PubMed: 28490441]
49. Wu D, Hu L, Han M, Deng Y, Zhang Y, Ren G, Zhao X, Li Z, Li P, Zhang Y, et al. (2022). PD-1 signaling facilitates activation of lymphoid tissue inducer cells by restraining fatty acid oxidation. Nat Metab 4, 867–882. 10.1038/s42255-022-00595-9. [PubMed: 35788761]
50. Vacca P, Pesce S, Greppi M, Fulcheri E, Munari E, Olive D, Mingari MC, Moretta A, Moretta L, and Marcenaro E (2019). PD-1 is expressed by and regulates human group 3 innate lymphoid cells in human decidua. Mucosal Immunol 12, 624–631. 10.1038/s41385-019-0141-9. [PubMed: 30755717]
51. Tumino N, Martini S, Munari E, Scordamaglia F, Besi F, Mariotti FR, Bogina G, Mingari MC, Vacca P, and Moretta L (2019). Presence of innate lymphoid cells in pleural effusions of primary and metastatic tumors: Functional analysis and expression of PD-1 receptor. Int J Cancer 145, 1660–1668. 10.1002/ijc.32262. [PubMed: 30856277]

52. Salimi M, Wang R, Yao X, Li X, Wang X, Hu Y, Chang X, Fan P, Dong T, and Ogg G (2018). Activated innate lymphoid cell populations accumulate in human tumour tissues. BMC Cancer 18, 341. 10.1186/s12885-018-4262-4. [PubMed: 29587679]
53. Bauche D, Joyce-Shaikh B, Jain R, Grein J, Ku KS, Blumenschein WM, Ganal-Vonarburg SC, Wilson DC, McClanahan TK, Malefyt RW, et al. (2018). LAG3(+) Regulatory T Cells Restrain Interleukin-23-Producing CX3CR1(+) Gut-Resident Macrophages during Group 3 Innate Lymphoid Cell-Driven Colitis. Immunity 49, 342–352 e345. 10.1016/j.immuni.2018.07.007. [PubMed: 30097293]
54. Zhang M, Zhou L, Xu Y, Yang M, Xu Y, Komaniecki GP, Kosciuk T, Chen X, Lu X, Zou X, et al. (2020). A STAT3 palmitoylation cycle promotes TH17 differentiation and colitis. Nature 586, 434–439. 10.1038/s41586-020-2799-2. [PubMed: 33029007]
55. Celada LJ, Kropski JA, Herazo-Maya JD, Luo W, Creecy A, Abad AT, Chioma OS, Lee G, Hassell NE, Shaginurova GI, et al. (2018). PD-1 up-regulation on CD4(+) T cells promotes pulmonary fibrosis through STAT3-mediated IL-17A and TGF-beta1 production. Sci. Transl. Med. 10. 10.1126/scitranslmed.aar8356.
56. Mezghiche I, Yahia-Cherbal H, Rogge L, and Bianchi E (2023). Interleukin 23 receptor: Expression and regulation in immune cells. Eur J Immunol, e2250348. 10.1002/eji.202250348. [PubMed: 37837262]
57. Pastor-Fernandez G, Mariblanca IR, and Navarro MN (2020). Decoding IL-23 Signaling Cascade for New Therapeutic Opportunities. Cells 9. 10.3390/cells9092044.
58. Saito-Sasaki N, Sawada Y, Mashima E, Yamaguchi T, Ohmori S, Yoshioka H, Haruyama S, Okada E, and Nakamura M (2018). Maresin-1 suppresses imiquimod-induced skin inflammation by regulating IL-23 receptor expression. Sci Rep 8, 5522. 10.1038/s41598-018-23623-9. [PubMed: 29615641]
59. Sun R, Hedl M, and Abraham C (2020). IL23 induces IL23R recycling and amplifies innate receptor-induced signalling and cytokines in human macrophages, and the IBD-protective IL23R R381Q variant modulates these outcomes. Gut 69, 264–273. 10.1136/gutjnl-2018-316830. [PubMed: 31097538]
60. McMahon HT, and Boucrot E (2011). Molecular mechanism and physiological functions of clathrin-mediated endocytosis. Nat Rev Mol Cell Biol 12, 517–533. 10.1038/nrm3151. [PubMed: 21779028]
61. Wang R, Zhang J, Li D, Liu G, Fu Y, Li Q, Zhang L, Qian L, Hao L, Wang Y, et al. (2022). Imbalance of circulating innate lymphoid cell subpopulations in patients with chronic kidney disease. Clin Immunol 239, 109029. 10.1016/j.clim.2022.109029. [PubMed: 35525476]
62. Doke T, Abedini A, Aldridge DL, Yang YW, Park J, Hernandez CM, Balzer MS, Shrestra R, Coppock G, Rico JMI, et al. (2022). Single-cell analysis identifies the interaction of altered renal tubules with basophils orchestrating kidney fibrosis. Nat Immunol 23, 947–959. 10.1038/s41590-022-01200-7. [PubMed: 35552540]
63. Law BM, Wilkinson R, Wang X, Kildey K, Lindner M, Beagley K, Healy H, and Kassianos AJ (2019). Effector gammadelta T cells in human renal fibrosis and chronic kidney disease. Nephrol Dial Transplant 34, 40–48. 10.1093/ndt/gfy098. [PubMed: 29897565]
64. Law BMP, Wilkinson R, Wang X, Kildey K, Giuliani K, Beagley KW, Ungerer J, Healy H, and Kassianos AJ (2019). Human Tissue-Resident Mucosal-Associated Invariant T (MAIT) Cells in Renal Fibrosis and CKD. J Am Soc Nephrol 30, 1322–1335. 10.1681/ASN.2018101064. [PubMed: 31186283]
65. Rezende RM, Lanser AJ, Rubino S, Kuhn C, Skillin N, Moreira TG, Liu S, Gabriely G, David BA, Menezes GB, and Weiner HL (2018). γδT cells control humoral immune response by inducing T follicular helper cell differentiation. Nat Commun 9, 3151. 10.1038/s41467-018-05487-9. [PubMed: 30089795]
66. Gnirck AC, Philipp MS, Waterholter A, Wunderlich M, Shaikh N, Adamiak V, Henneken L, Kautz T, Xiong T, Klaus D, et al. (2023). Mucosal-associated invariant T cells contribute to suppression of inflammatory myeloid cells in immune-mediated kidney disease. Nat Commun 14, 7372. 10.1038/s41467-023-43269-0. [PubMed: 37968302]

67. Pentcheva-Hoang T, Chen L, Pardoll DM, and Allison JP (2007). Programmed death-1 concentration at the immunological synapse is determined by ligand affinity and availability. Proc Natl Acad Sci U S A 104, 17765–17770. 10.1073/pnas.0708767104. [PubMed: 17968013]
68. Huang Y, Mao K, Chen X, Sun MA, Kawabe T, Li W, Usher N, Zhu J, Urban JF Jr., Paul WE, and Germain RN (2018). S1P-dependent interorgan trafficking of group 2 innate lymphoid cells supports host defense. Science 359, 114–119. 10.1126/science.aam5809. [PubMed: 29302015]
69. Matha L, Romera-Hernandez M, Steer CA, Yin YH, Orangi M, Shim H, Chang C, Rossi FM, and Takei F (2021). Migration of Lung Resident Group 2 Innate Lymphoid Cells Link Allergic Lung Inflammation and Liver Immunity. Front Immunol 12, 679509. 10.3389/fimmu.2021.679509. [PubMed: 34305911]
70. Stavropoulou E, Kantartzi K, Tsigalou C, Konstantinidis T, Romanidou G, Voidarou C, and Bezirtzoglou E (2020). Focus on the Gut-Kidney Axis in Health and Disease. Front Med (Lausanne) 7, 620102. 10.3389/fmed.2020.620102. [PubMed: 33553216]
71. Meijers B, Evenepoel P, and Anders HJ (2019). Intestinal microbiome and fitness in kidney disease. Nat Rev Nephrol 15, 531–545. 10.1038/s41581-019-0172-1. [PubMed: 31243394]
72. Yang T, Richards EM, Pepine CJ, and Raizada MK (2018). The gut microbiota and the brain-gut-kidney axis in hypertension and chronic kidney disease. Nat Rev Nephrol 14, 442–456. 10.1038/s41581-018-0018-2. [PubMed: 29760448]
73. Fellström BC, Barratt J, Cook H, Coppo R, Feehally J, de Fijter JW, Floege J, Hetzel G, Jardine AG, Locatelli F, et al. (2017). Targeted-release budesonide versus placebo in patients with IgA nephropathy (NEFIGAN): a double-blind, randomised, placebo-controlled phase 2b trial. The Lancet 389, 2117–2127. 10.1016/s0140-6736(17)30550-0.
74. Peng X, Wang Y, Li H, Fan J, Shen J, Yu X, Zhou Y, and Mao H (2019). ATG5-mediated autophagy suppresses NF-kappaB signaling to limit epithelial inflammatory response to kidney injury. Cell Death Dis 10, 253. 10.1038/s41419-019-1483-7. [PubMed: 30874544]
75. Stack EC, Wang C, Roman KA, and Hoyt CC (2014). Multiplexed immunohistochemistry, imaging, and quantitation: a review, with an assessment of Tyramide signal amplification, multispectral imaging and multiplex analysis. Methods 70, 46–58. 10.1016/j.ymeth.2014.08.016. [PubMed: 25242720]
76. Chen S, Zhou Y, Chen Y, and Gu J (2018). fastp: an ultra-fast all-in-one FASTQ preprocessor. Bioinformatics 34, i884–i890. 10.1093/bioinformatics/bty560. [PubMed: 30423086]
77. Smith T, Heger A, and Sudbery I (2017). UMI-tools: modeling sequencing errors in Unique Molecular Identifiers to improve quantification accuracy. Genome Res 27, 491–499. 10.1101/gr.209601.116. [PubMed: 28100584]
78. Dobin A, Davis CA, Schlesinger F, Drenkow J, Zaleski C, Jha S, Batut P, Chaisson M, and Gingeras TR (2013). STAR: ultrafast universal RNA-seq aligner. Bioinformatics 29, 15–21. 10.1093/bioinformatics/bts635. [PubMed: 23104886]
79. Becker GJ, and Hewitson TD (2009). Kidney Research: Experimental Protocols (Springer).
80. Jumper J, Evans R, Pritzel A, Green T, Figurnov M, Ronneberger O, Tunyasuvunakool K, Bates R, Zidek A, Potapenko A, et al. (2021). Highly accurate protein structure prediction with AlphaFold. Nature 596, 583–589. 10.1038/s41586-021-03819-2. [PubMed: 34265844]

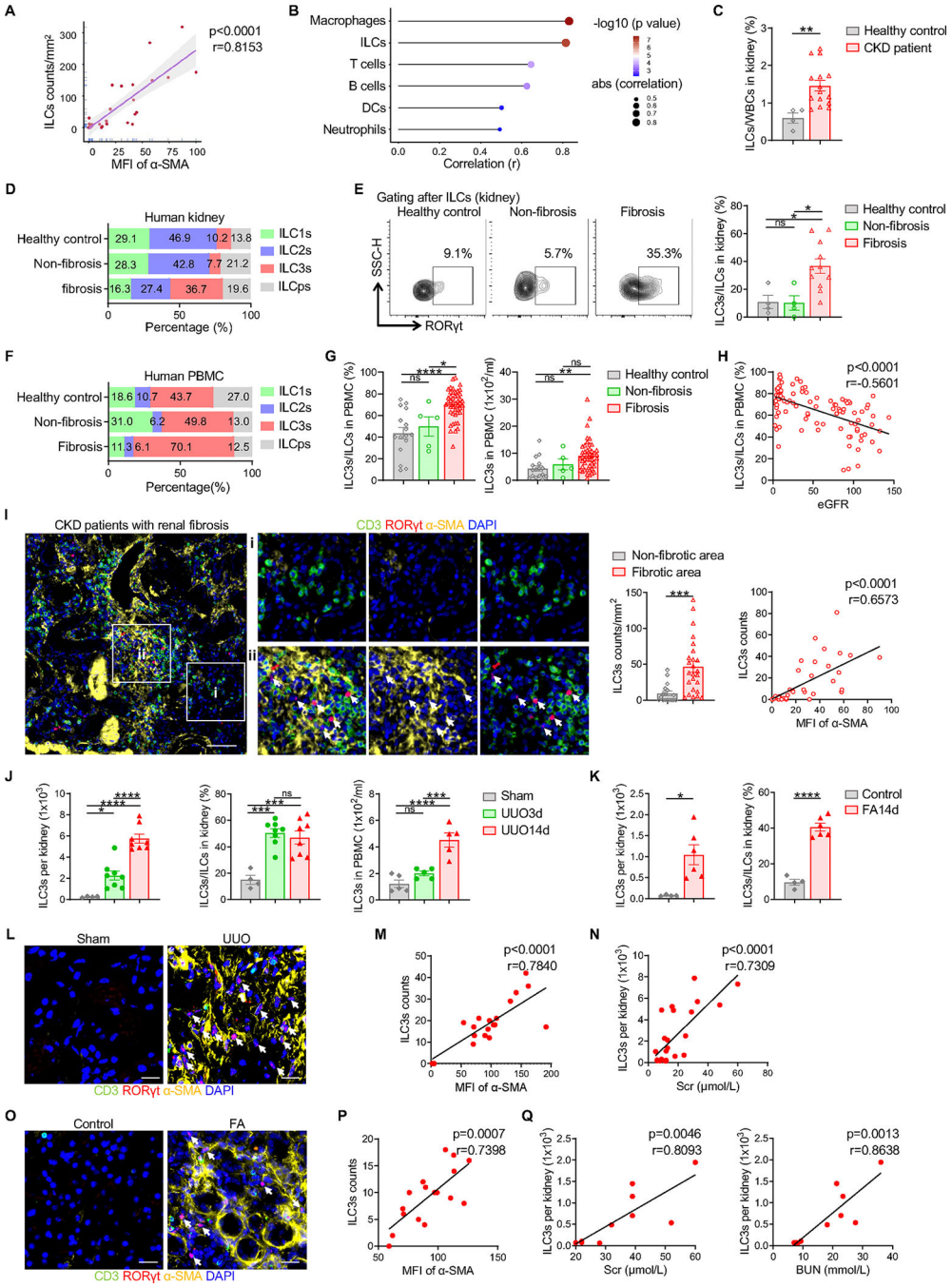

Figure 1. ILC3s accumulate in human and mouse renal fibrosis

(A-B) CKD patients' kidney biopsies were divided into different regions according to α-SMA expression. Relationships between α-SMA MFI and immune cells' density in these areas (n = 30) were analyzed. The Lollipop chart shows the correlation index and p value. The etiologies of CKD patients include IgA Nephropathy (IgAN), Membranous Nephropathy (MN), and Lupus Nephritis (LN).

(C-E) Percentages of ILCs within total white blood cells (WBCs) and ILC subsets among ILCs in kidneys of HCs (n = 4) and CKD patients with or without renal fibrosis (n = 15).

(F-G) Percentages of ILC subsets among ILCs and absolute number of ILC3s in PBMC of HCs (n = 16) and CKD patients with or without renal fibrosis (n = 51).
(H) Correlation between ILC3s percentage among ILCs in PBMC and eGFR (ml/min/1.73m^2) of HCs (n = 16) and CKD patients (n = 80).
(I) Multiplex immunofluorescence staining of CKD patients' kidney biopsies with CD3, RORγt, α-SMA and DAPI. Scale bars, 50 μm. The sections were divided into fibrotic areas and non-fibrotic areas according to α-SMA expression, and ILC3s counts in these areas were compared (n = 42). Relationship between α-SMA MFI and ILC3s counts in these areas was analyzed. The etiologies of CKD patients include IgAN, MN, and LN.
(J) Absolute number and percentage of renal ILC3s, and concentration of circulating ILC3s in sham and UUO mice were examined by flow cytometry (n = 4–8 per group).
(K) Absolute number and percentage of renal ILC3s in vehicle-treated control (n = 4) and FA14d mice were examined by flow cytometry (n = 6).
(L-M) Immunofluorescence staining of CD3, RORγt, α-SMA, and DAPI in sham or UUO14d mice kidneys (L). White arrows indicate CD3$^-$RORγt$^+$ ILC3s.Scale bars, 50 μm. Relationship between α-SMA MFI and renal ILC3s number (n = 19) was analyzed (M).
(N) Relationship between serum creatinine level (Scr) and renal ILC3s number in sham and UUO mice (n = 24).
(O-P) Immunofluorescence staining of CD3, RORγt, α-SMA, and DAPI in vehicle-treated control and FA14d mice kidneys (O). White arrows indicate CD3$^-$RORγt$^+$ ILC3s. Scale bars, 50 μm. Relationship between α-SMA MFI and renal ILC3s number (n = 17) was analyzed (P).
(Q) Relationships between Scr and blood urea nitrogen (BUN) with renal ILC3s number in vehicle-treated control and FA14d mice (n = 9).
Data are pooled from or representative of two to four independent experiments and shown as mean ± SEM. Each symbol in C, E, G, H, J, K, N and Q represents an individual human or mouse. Each symbol in I, M and P represents an individual area or slide. Student's t test (C, I (left), K), one-way ANOVA test (E, G, J) and Pearson's correlation test (A, H, I (right), M, N, P, Q) were performed. ****p < 0.0001; ***p < 0.001; **p < 0.01; *p < 0.05; ns, not significant.
See also Figure S1 and Tables S1–S3.

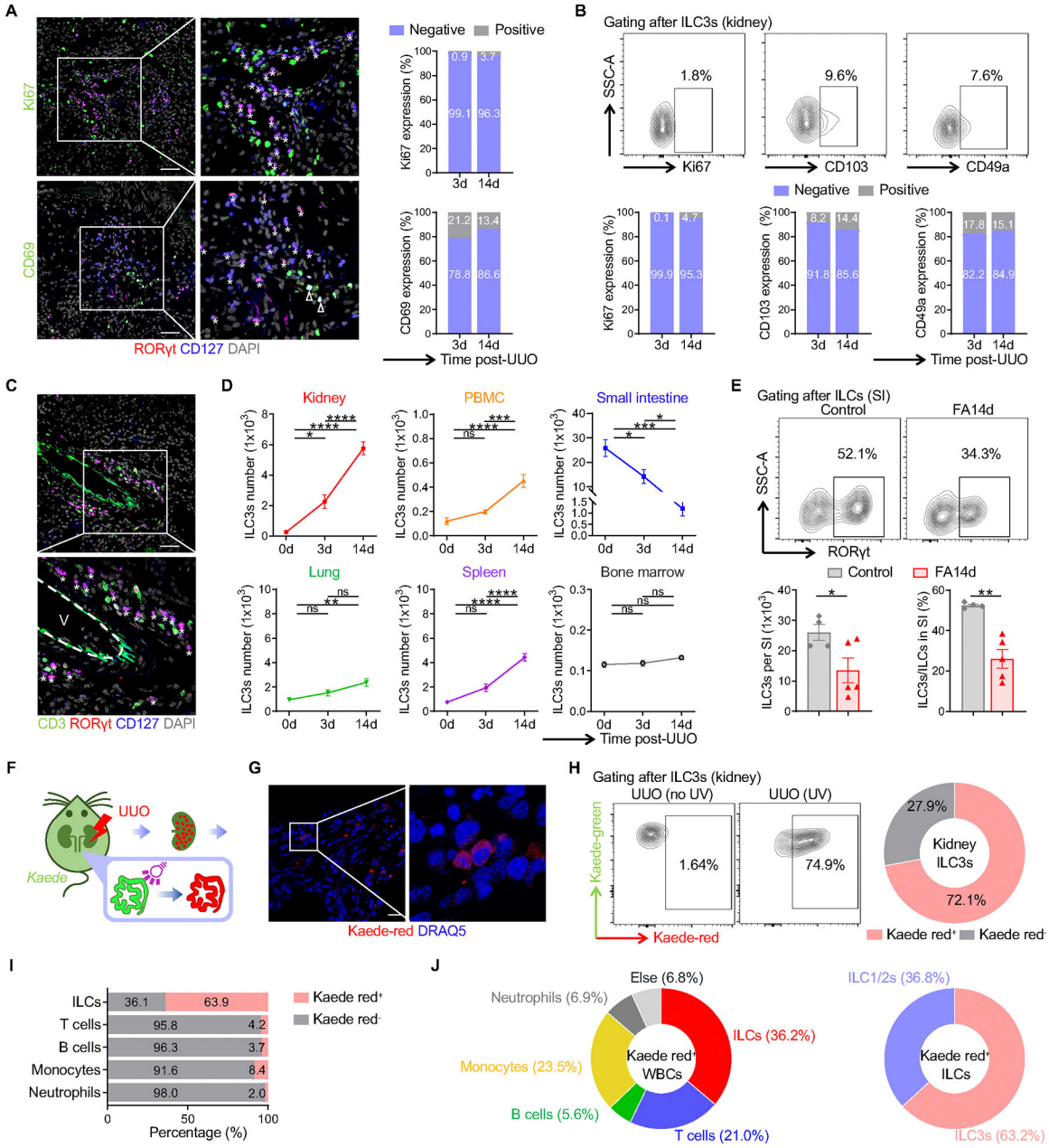

Figure 2. Intestine-derived ILC3s rapidly accumulate in fibrotic kidney

(A) Representative immunofluorescence staining of Ki67 or CD69, RORγt, CD127, and DAPI in UUO3d kidneys. ILC3s are indicated as CD127$^+$ RORγt$^+$. White stars indicate Ki67$^-$ or CD69$^-$ ILC3s. Open white triangles indicate Ki67$^+$ or CD69$^+$ ILC3s. Scale bars, 50 μm. ILC3 expression of Ki67and CD69 in UUO3d and UUO14d kidneys was quantified (n = 5 per group).

(B) Expression of Ki67, CD103, and CD49a on ILC3s in obstructed kidneys (n = 5 per group).

(C) Immunofluorescence staining of UUO3d kidneys with CD3, RORγt, CD127 and DAPI. White stars indicate $CD3^{-}CD127^{+}ROR\gamma t^{+}$ ILC3s. "V" indicates blood vessels. Scale bars, 50 μm.

(D) ILC3s in UUO mice kidneys, PBMC, small intestines (SI), lungs, spleens and bone marrow (n = 4–8 per group).

(E) SI-ILC3s in vehicle-treated control (n = 4) or FA14d mice (n = 5).

(F) *Kaede* transgenic mice SI were photoconverted (green to red) immediately before UUO, and the migration of cells to the kidney was examined at UUO3d.

(G) Confocal microscopy of Kaede red^{+} cells in *Kaede*-UUO mice kidneys. Cell nuclei were counterstained with DRAQ5. Scale bars, 20 μm.

(H) Kaede-red expression in renal ILC3s of *Kaede*-UUO mice with or without intestinal photoconversion (n = 3 per group).

(I) Kaede-red expression in renal ILCs, T cells, B cells, monocytes and neutrophils of *Kaede*-UUO mice with intestinal photoconversion (n = 3).

(J) Kaede red^{+} immune cell proportions among total Kaede red^{+} cells in intestine-photoconverted *Kaede*-UUO mice kidneys (n = 3).

Data are pooled from or representative of two to four independent experiments and shown as mean ± SEM. Each symbol in E represents an individual mouse. One-way ANOVA test (D) and Student's t test (E), were performed. ****p < 0.0001; ***p < 0.001; **p < 0.01; *p < 0.05; ns, not significant.

See also Figure S2.

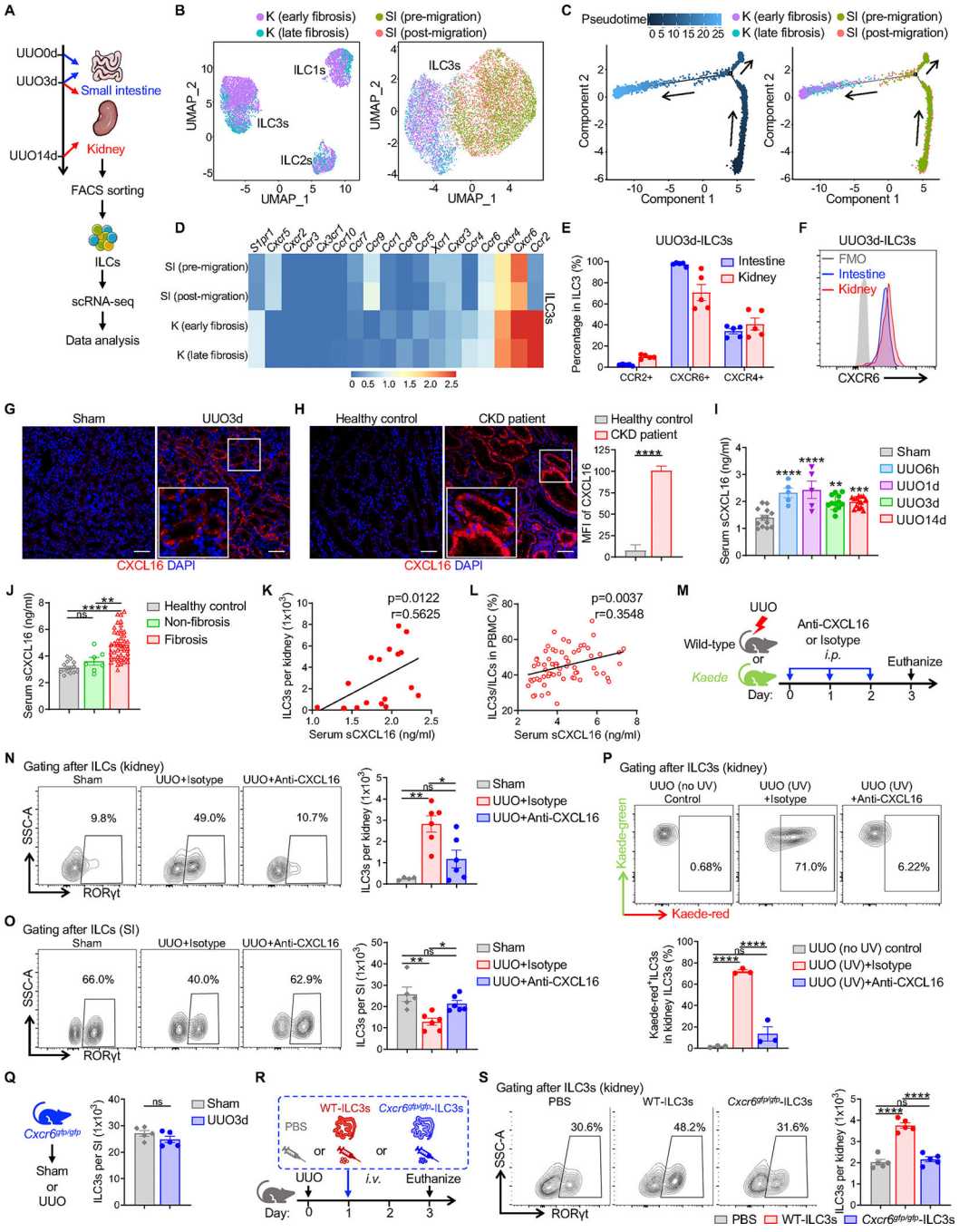

Figure 3. Intestinal ILC3s migrate into injured kidney via CXCR6-CXCL16 axis

(A) Strategy for scRNA-seq.

(B) ILC subsets in kidney (left) and ILC3s in intestine and kidney (right) were analyzed by UMAP.

(C) Unsupervised transcriptional trajectory of intestinal and renal ILC3s, colored by cell pseudo-time and samples.

(D) Heatmap showing chemokine receptors in renal and intestinal ILC3s.

(E-F) Expression of CCR2, CXCR6 and CXCR4 on ILC3s in UUO3d mice intestines or kidneys (n = 5 per group) were measured by flow cytometry.
(G) Confocal images of mice kidneys with CXCL16. Scale bars, 50 μm.
(H) Confocal images of human kidneys with CXCL16, CXCL16 expression in the kidneys of HCs (n = 3) and CKD patients (n = 5) were compared. Scale bars, 50 μm.
(I-J) Serum sCXCL16 in mice (n = 5–14 per group) (I) and human (HCs, n = 15; non-fibrosis, n = 7; fibrosis, n = 43) (J) were detected with ELISA.
(K-L) Relationships between serum sCXCL16 with ILC3s counts in UUO mice kidneys (n = 19) (K), and frequency of ILC3s in patients' PBMC (n = 65) (L).
(M) Experimental design for (N-P).
(N-P) ILC3s in kidneys (N) and intestines (O) of WT-UUO mice (n = 4–6 per group), and Kaede red$^+$ ILC3s in *Kaede*-UUO mice (n = 3 per group) (P) were measured by flow cytometry.
(Q) SI-ILC3s in *Cxcr6*$^{gfp/gfp}$-sham and *Cxcr6*$^{gfp/gfp}$-UUO3d mice were analyzed by flow cytometry (n = 5 per group).
(R) Experimental design for (S).
(S) Kidney ILC3s were measured by flow cytometry (n = 5 per group).
Data are pooled from or representative of two to four independent experiments and shown as mean ± SEM. Each symbol in E, I, J-L, N-Q and S represents an individual human or mouse. Student's t test (H, Q), one-way ANOVA test (I, J, N-P, S) and Pearson's correlation test (K, L) were performed. ****p < 0.0001; ***p < 0.001; **p < 0.01; *p < 0.05; ns, not significant.
See also Figure S3.

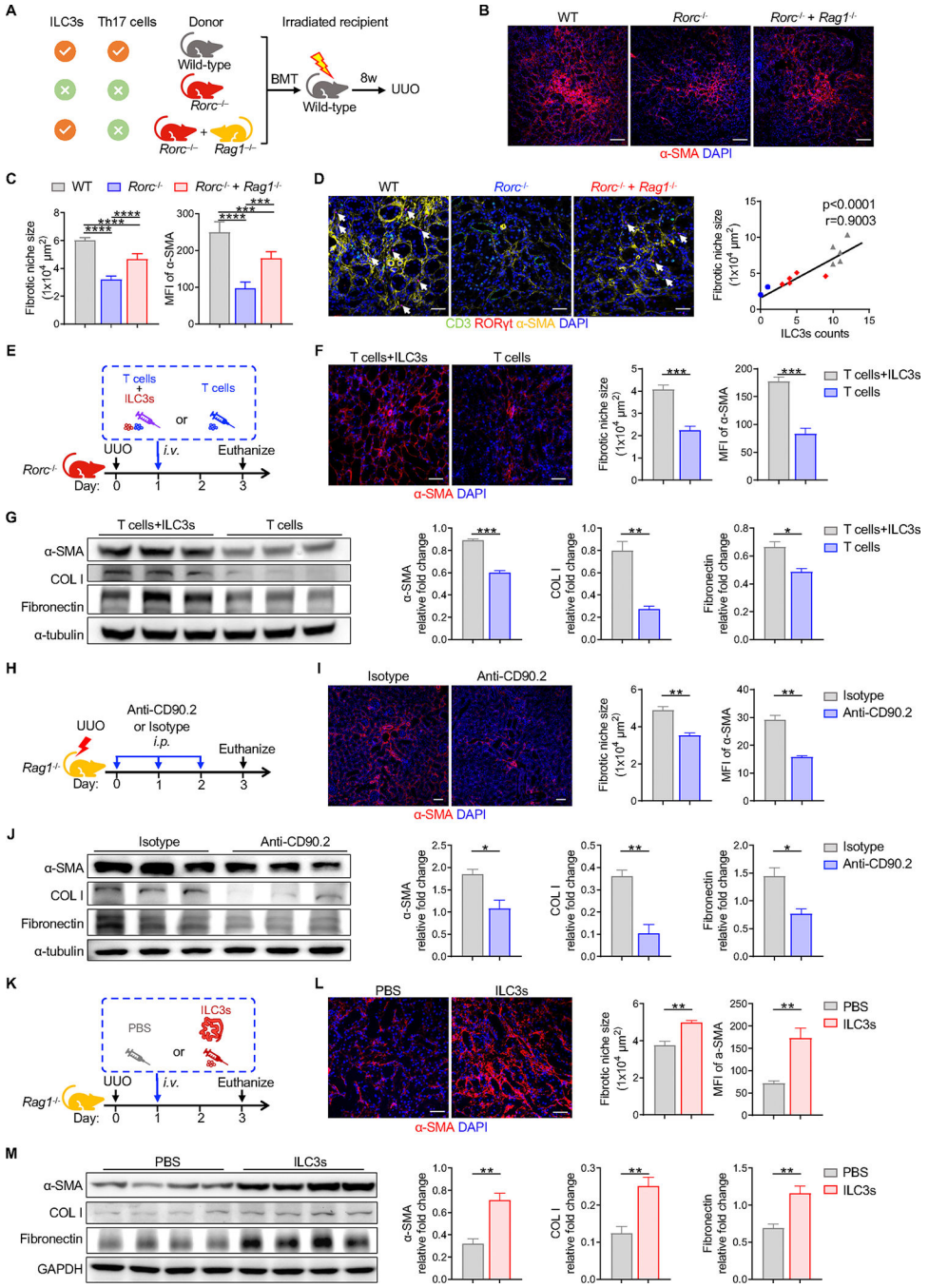

Figure 4. ILC3s mediate fibrotic niche formation and contribute to renal fibrosis

(A) Experimental design for (B-D).

(B-C) Immunofluorescence staining of α-SMA and DAPI in kidneys (B). Scale bars, 100 μm. Fibrotic niche size (α-SMA) and α-SMA MFI were compared (n = 5 per group) (C).

(D) Immunofluorescence staining of CD3, RORγt, α-SMA and DAPI in kidneys. Scale bars, 50 μm. White arrows indicate $CD3^{-}ROR\gamma t^{+}$ ILC3s. Relationship between fibrotic niche sizes (α-SMA) and ILC3 numbers in fibrotic niches was analyzed.

(E) Experimental design for (F-G).

(F) Immunofluorescence staining of α-SMA and DAPI in kidneys. Scale bars, 50 μm. Fibrotic niche sizes (α-SMA) and α-SMA MFI were compared (n = 5 per group).
(G) Kidney expression of α-SMA, collagen I (COL I) and fibronectin was determined by Western blot (n = 3 per group).
(H) Experimental design for (I-J).
(I) Immunofluorescence staining of α-SMA and DAPI in kidneys. Scale bars, 50 μm. Fibrotic niche sizes (α-SMA) and α-SMA MFI were compared (n = 3 per group).
(J) Kidney expression of α-SMA, COL I and fibronectin was determined by Western blot (n = 3 per group).
(K) Experimental design for (L-M).
(L) Immunofluorescence staining of α-SMA and DAPI in mice kidneys. Scale bars, 50 μm. Fibrotic niche sizes (α-SMA) and α-SMA MFI were compared (n = 4 per group).
(M) Kidney expression of α-SMA, COL I and fibronectin was determined by Western blot (n = 4 per group).
Data are pooled from or representative of two to four independent experiments and shown as mean ± SEM. Each symbol in D represents an individual mouse. Student's t test (F, G, I, J, L, M), one-way ANOVA test (C) and Pearson's correlation test (D) were performed. ****p < 0.0001; ***p < 0.001; **p < 0.01; *p < 0.05.
See also Figure S4.

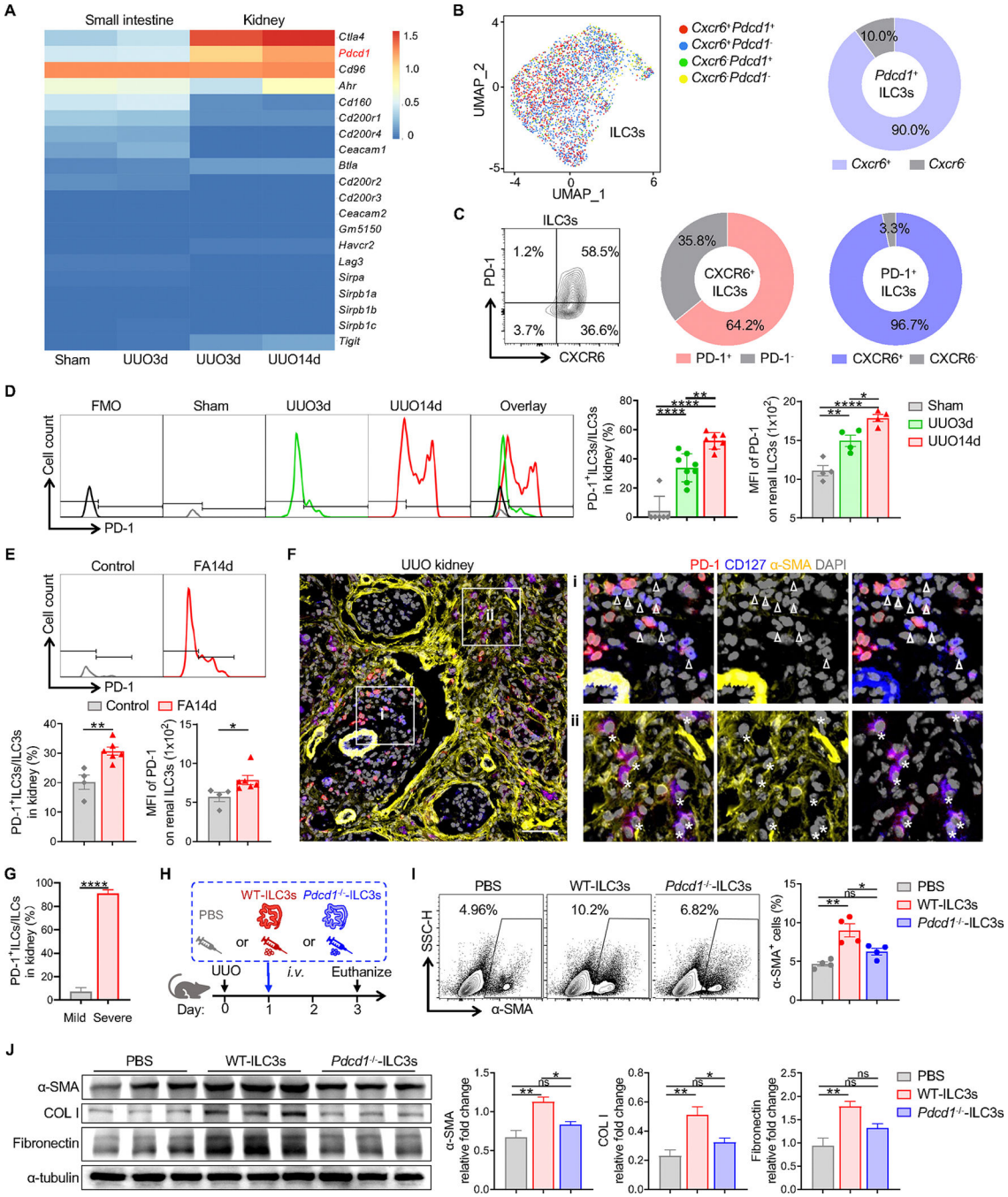

Figure 5. Elevated PD-1 expression enhanced the pro-fibrotic role of kidney-infiltrating ILC3s

(A) Heatmap showing immune checkpoints in intestinal and renal ILC3s.

(B) scRNA-seq data showing *Cxcr6* expression on *Pdcd1*-positive ILC3s.

(C) PD-1 and CXCR6 expression on renal ILC3s in UUO14d mice ($n = 5$).

(D) PD-1 MFI on renal ILC3s and PD-1$^+$ ILC3s percentage among ILC3s between sham and UUO mice ($n = 4$–8 per group).

(E) PD-1 MFI on renal ILC3s and PD-1$^+$ ILC3s percentage among ILC3s in vehicle-treated control ($n = 4$) and FA14d mice ($n = 6$).

(F-G) Immunofluorescence staining of α-SMA, CD127, PD-1 and DAPI in UUO14d kidneys (F). ILCs are indicated as $CD127^+$. Scale bars, 50 μm. White stars indicate $PD\text{-}1^+$ ILCs. Open white triangles indicate $PD\text{-}1^-$ ILCs. Area (i) and (ii) represent areas with mild or severe fibrosis respectively. $PD\text{-}1^+$ ILCs frequency among ILCs in areas with mild fibrosis ($n = 3$) or severe fibrosis ($n = 4$) was compared (G).

(H) Experimental design for (I-J).

(I) Percentage of myofibroblasts ($\alpha\text{-}SMA^+$) in kidneys was measured by flow cytometry ($n = 4$ per group).

(J) Kidney expression of α-SMA, COL I and fibronectin was determined by Western blot ($n = 3$ per group).

Data are pooled from or representative of two to four independent experiments and shown as mean ± SEM. Each symbol in D, E and I represents an individual mouse. One-way ANOVA test (D, I, J) and Student's *t* test (E, G) were performed. ****$p < 0.0001$; **$p < 0.01$; *$p < 0.05$; ns, not significant.

See also Figure S5.

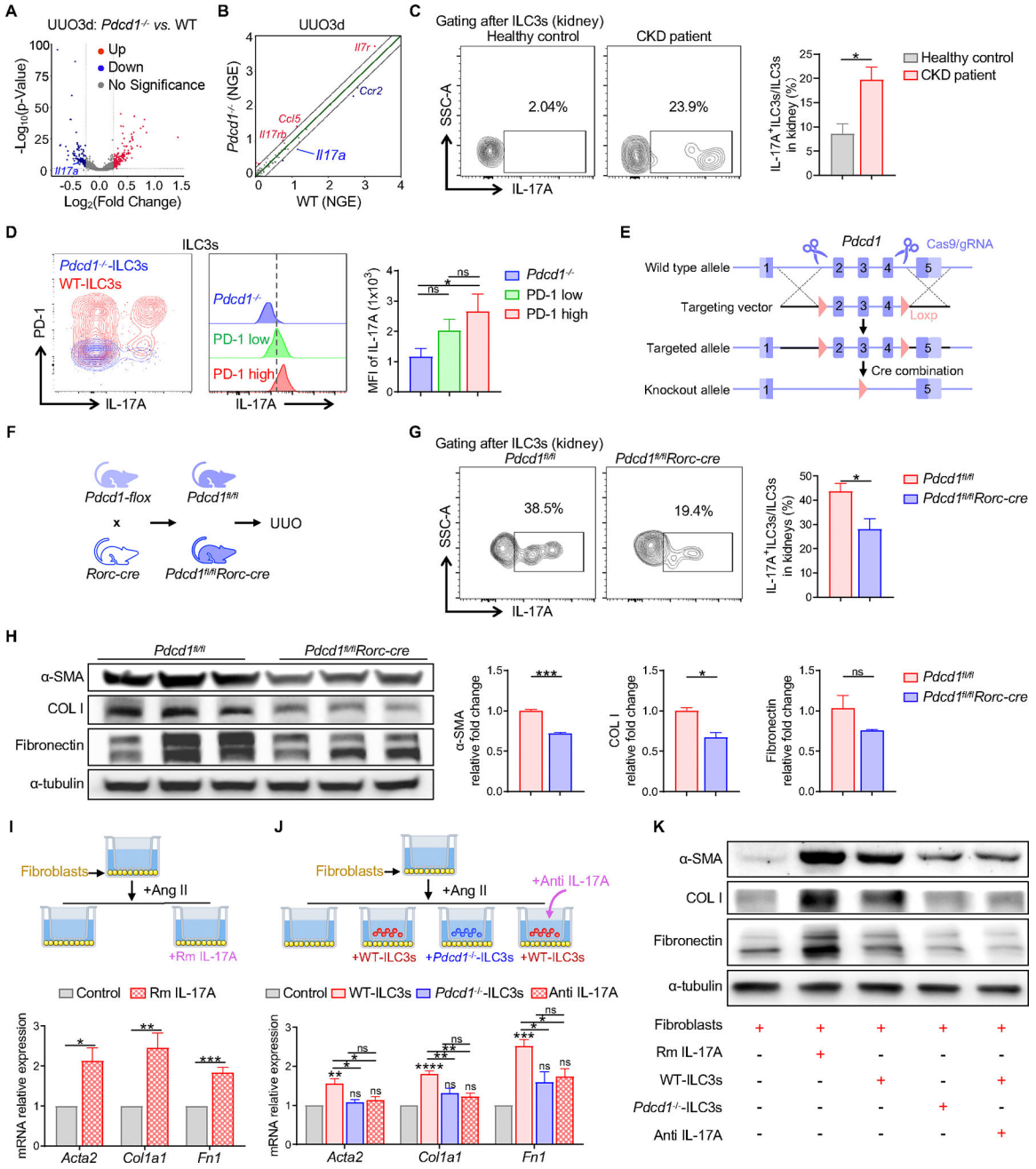

Figure 6. PD-1 on ILC3s increases IL-17A production to enhance fibroblasts activation

(A) Differentially regulated genes between renal ILC3s of WT-UUO3d and *Pdcd1*$^{-/-}$-UUO3d mice.

(B) Differentially expressed cytokine genes in *Pdcd1*$^{-/-}$- UUO3d-ILC3s compared to WT-UUO3d-ILC3s. The x and y axes show the Normalization Gene Expression (NGE) for each group, and Genes above the diagonal are increased and those below are decreased in *Pdcd1*$^{-/-}$-UUO3d-ILC3s. Genes outside the gray area are differentially expressed.

(C-D) The renal cell suspension was stimulated with cell stimulation cocktails (eBioscience) and IL-17A expression in renal ILC3s of HCs and CKD patients (n = 5 per group) (C), and

WT-UUO3d and *Pdcd1*$^{-/-}$-UUO3d mice were detected by flow cytometry and compared (D) (*n* = 3 per group).

(E) Schematic of *Pdcd1* targeting strategy.

(F) Schematic of generation PD-1 conditional deletion mice and experimental design.

(G) The renal cell suspension was stimulated with cell stimulation cocktails (eBioscience) and IL-17A expression in renal ILC3s of *Pdcd1*$^{fl/fl}$-UUO3d and *Pdcd1*$^{fl/fl}$*Rorc-cre*-UUO3d mice were detected by flow cytometry and compared (*n* = 3–4 per group).

(H) Expression of α-SMA, COL I and fibronectin in *Pdcd1*$^{fl/fl}$-UUO3d and *Pdcd1*$^{fl/fl}$*Rorc-cre*-UUO3d mice kidneys were determined by Western blot (*n* = 3 per group).

(I-K) Primary renal fibroblasts were cultured alone, stimulated with rmIL-17A or cocultured with WT-ILC3, *Pdcd1*$^{-/-}$ -ILC3s for 24h or 48h. The neutralizing anti-IL-17A antibody was added in some systems (*n* = 4–6 per group). The expression of α-SMA, COL I and fibronectin by fibroblasts was determined by real-time PCR (GAPDH was the standard) or Western blot.

Data are pooled from or representative of two to four independent experiments and shown as mean ± SEM. One-way ANOVA test (D, J) and Student's *t* test (C, G, H, I) were performed. ****p < 0.0001; ***p < 0.001; **p < 0.01; *p < 0.05; ns, not significant.

See also Figure S6 and Table S4.

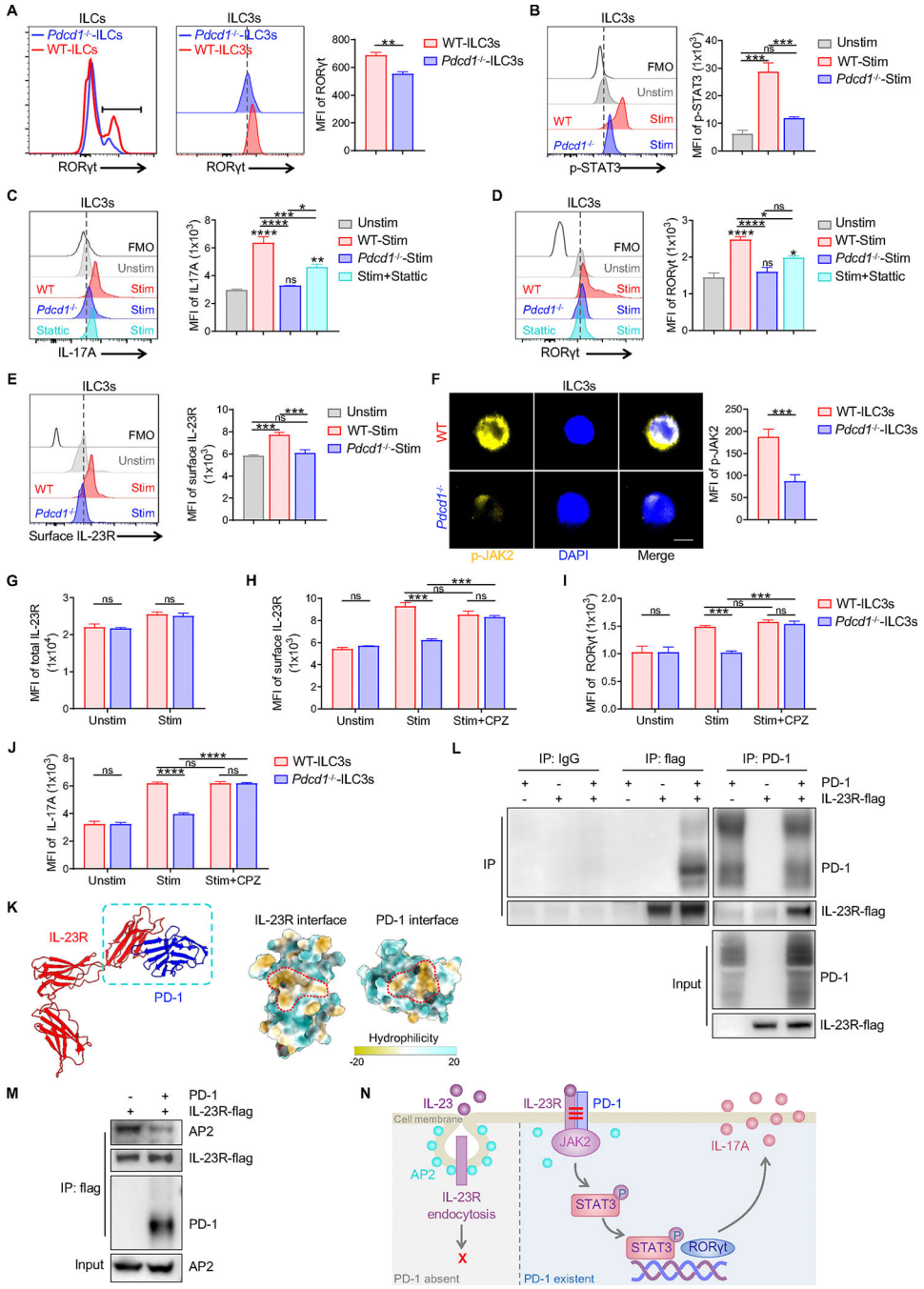

Figure 7. PD-1 amplifies IL-23-induced JAK2/STAT3/RORγt/IL-17A signaling in ILC3s by competitively binding IL-23R to inhibit endocytosis.

(A) RORγt expression of renal ILC3s from WT-UUO3d and *Pdcd1*$^{-/-}$-UUO3d mice were compared by flow cytometry (n = 3 per group).

(B) WT-ILC3s and *Pdcd1*$^{-/-}$-ILC3s were cultured alone or stimulated with IL-23/IL-1β for 20 min. p-STAT3 expression was measured by flow cytometry (n = 2–6 per group).

(C-D) WT-ILC3s and *Pdcd1*$^{-/-}$-ILC3s were activated by IL-23/IL-1β with or without Stattic for 48h. IL-17A (C) and RORγt expression (D) on ILC3s were measured by flow cytometry (n = 2–11 per group).

(E-G) WT-ILC3s and *Pdcd1*$^{-/-}$-ILC3s were activated by IL-23/IL-1β for 2h or 48h. Surface IL-23R (E), p-JAK2 (F) and total IL-23R (G) were detected with flow cytometry or immunofluorescence (n = 3–9 per group).
(H-J) WT-ILC3s and *Pdcd1*$^{-/-}$-ILC3s were preincubated for 30 min in the medium with or without chlorpromazine (CPZ), and then activated by IL-23 for 2h or 48h. Surface IL-23R (H), RORγt (I) and IL-17A (J) were detected by flow cytometry (n = 3 per group).
(K) Structural prediction of PD-1 and IL-23R protein combination with AlphaFold2. The interfaces were colored by hydrophobicity. Yellow means hydrophobic and blue means hydrophilic. The sites of hydrophobic interactions were outlined by red dotted lines.
(L-M) Co-immunoprecipitation of PD-1, IL-23R-3×FLAG, and AP2 in HEK-293T.
(N) Schematic of PD-1 mechanism in ILC3s.
Data are pooled from or representative of two to four independent experiments and shown as mean ± SEM. Student's t test (A, F-J) and One-way ANOVA test (B-E) were performed. ****p < 0.0001; ***p < 0.001; **p < 0.01; *p < 0.05; ns, not significant.
See also Figure S7.

Key resources table

REAGENT or RESOURCE	SOURCE	IDENTIFIER
Antibodies		
Mouse anti-GAPDH (clone 6C5)	Abcam	Cat#ab8245; RRID: AB_2107448
Mouse monoclonal anti-α-Tubulin (clone DM1A)	CST	Cat#12351S; AB_2797891
Mouse monoclonal anti-α-SMA (clone 1A4)	Sigma-Aldrich	Cat#A5228; RRID: AB_262054
Rabbit polyclonal anti-Fibronectin	BOSTER	Cat#BA1772; RRID: AB_3065025
Rabbit polyclonal anti-COL1A1	BOSTER	Cat#BA0325; RRID: AB_2891224
Rabbit polyclonal anti-FLAG	Proteintech	Cat# 20543-1-AP; RRID: AB_11232216
Rabbit polyclonal anti-IgG control	Proteintech	Cat#30000-0-AP; RRID: AB_10265197
Mouse monoclonal anti-AP2 (clone AP6)	Invitrogen	Cat#MA1-064; RRID: AB_2258307
PE anti-human CD45 (clone 2D1)	Biolegend	Cat#368509; RRID: AB_2566369
APC/Fire™ 750 anti-human CD45 (clone HI30)	Biolegend	Cat#304061; RRID: AB_2629700
Pacific Blue™ anti-human CD127 (clone A019D5)	Biolegend	Cat#351306; RRID: AB_10718638
FITC anti-human CD3ε (clone OKT3)	Biolegend	Cat#317306; RRID: AB_571905
FITC anti-human CD14 (clone HCD14)	Biolegend	Cat#325604; RRID: AB_830677
FITC anti-human CD11c (clone 3.9)	Biolegend	Cat#301604; RRID: AB_314174
FITC anti-human CD19 (clone HIB19)	Biolegend	Cat#302206; RRID: AB_314236
Brilliant Violet 605™ anti-human CD56 (clone 5.1H11)	Biolegend	Cat#362538; RRID: AB_2565856
APC/Cyanine7 anti-human CRTH2 (clone BM16)	Biolegend	Cat#350114; RRID: AB_2562465
PE/Cyanine7 anti-human CD117 (clone 104D2)	eBioscience	Cat#25-1178-42; RRID: AB_10718535
APC anti-human ROR gamma (t) (clone AFKJS-9)	eBioscience	Cat#17-6988-82; RRID: AB_10609207
PE anti-human IL-17A (clone eBio64DEC17)	eBioscience	Cat# 12-7179-42; RRID: AB_1724136
PE/Cyanine7 anti-human CXCR6 (clone K041E5)	Biolegend	Cat#356012; RRID: AB_2562315
APC/Fire™ 750 anti-mouse CD45 (clone 30-F11)	Biolegend	Cat#103154; RRID: AB_2572116
PE/Cyanine7 anti-mouse CD127 (clone A7R34)	Biolegend	Cat#135014; RRID: AB_1937265
FITC anti-mouse CD3ε (clone 145-2C11)	Biolegend	Cat#100306; RRID: AB_312671
FITC anti-mouse B220 (clone RA3-6B2)	Biolegend	Cat#103205; RRID: AB_312990
FITC anti-mouse CD11b (clone M1/70)	Biolegend	Cat#103205; RRID: AB_312990
FITC anti-mouse Ly6G/Ly6C(Gr-1) (clone RB6-8C5)	Biolegend	Cat#108405; RRID: AB_313370
FITC anti-mouse TER119 (clone TER-119)	Biolegend	Cat#116206; RRID: AB_313707
PE/Cyanine7 anti-mouse CD3ε (clone 145-2C11)	Biolegend	Cat#100320; RRID: AB_312685
PE/Cyanine7 anti-mouse B220 (clone RA3-6B2)	Biolegend	Cat#103221; RRID: AB_313004
PE/Cyanine7 anti-mouse CD11b (clone M1/70)	Biolegend	Cat#101215; RRID: AB_312799
PE/Cyanine7 anti-mouse Ly6G/Ly6C(Gr-1) (clone RB6-8C5)	Biolegend	Cat#108415; RRID: AB_313380
PE/Cyanine7 anti-mouse TER119 (clone TER-119)	Biolegend	Cat#116221; RRID: AB_2137789
Brilliant Violet 421 ™ anti-mouse CD127 (clone A7R34)	Biolegend	Cat#135024; RRID: AB_11218800
Brilliant Violet 711™ anti-mouse CD127 (clone A7R34)	Biolegend	Cat#135035; RRID: AB_2564577
PE anti-mouse CD117 (clone 2B8)	Biolegend	Cat#105808; RRID: AB_313217

REAGENT or RESOURCE	SOURCE	IDENTIFIER
APC/Cyanine7 anti-mouse CD11b (clone M1/70)	Biolegend	Cat#101226; RRID: AB_830642
Alexa Fluor® 700 anti-mouse CD3 (clone 17A2)	Biolegend	Cat#100216; RRID: AB_493697
Super Bright™ 600 anti-mouse CD11b (clone M1/70)	eBioscience	Cat# 63-0112-82; RRID: AB_2637408
APC anti-mouse Ly6G (clone 1A8)	Biolegend	Cat#127614; RRID: AB_2227348
Brilliant Violet 510™ anti-mouse B220 (clone RA3-6B2)	Biolegend	Cat#103248; RRID: AB_2650679
APC anti-mouse PD-1 (clone RMP1-30)	Biolegend	Cat#109112; RRID: AB_10612938
PE anti-mouse PD-1 (clone RMP1-30)	Biolegend	Cat#109104; RRID: AB_313421
Brilliant Violet 605™ anti-mouse CD69 (clone H1.2F3)	Biolegend	Cat#104530; RRID: AB_2563062
Brilliant Violet 605™ anti-mouse CD103 (clone 2E7)	Biolegend	Cat#121433; RRID: AB_2629724
PE anti-mouse CD49a (clone HMα1)	Biolegend	Cat#142604; RRID: AB_10945158
APC anti-mouse CXCR6 (clone SA051D1)	Biolegend	Cat#151106; RRID: AB_2572143
Brilliant Violet 421 ™ anti-mouse CXCR4 (clone L276F12)	Biolegend	Cat#146511; RRID: AB_2562788
PE anti-mouse CCR2 (clone SA203G11)	Biolegend	Cat#150609; RRID: AB_2616981
FITC anti-mouse CD4 (clone GK1.5)	Biolegend	Cat#100406; RRID: AB_312691
PE/Cyanine7 anti-mouse CD4 (clone GK1.5)	Biolegend	Cat#100422; RRID: AB_312707
PE anti-mouse F4/80 (clone BM8)	eBioscience	Cat#12-4801-82; RRID: AB_465923
APC anti-mouse Ki67 (clone SolA15)	eBioscience	Cat#17-5698-82; RRID: AB_2688057
APC anti-mouse CD45.1 (clone A20)	Biolegend	Cat#110714; RRID: AB_313503
PE anti-mouse CD45.1 (clone A20)	Biolegend	Cat#110707; RRID: AB_313496
APC anti-mouse CD45.2 (clone 104)	Biolegend	Cat#109814; RRID: AB_389211
Brilliant Violet 421 ™ anti-mouse IL-17A (clone TC11-18H10.1)	Biolegend	Cat#506925; RRID: AB_10900442
Brilliant Violet 421 ™ anti-mouse IL-23R (clone 12B2B64)	Biolegend	Cat#150907; RRID: AB_2715804
APC anti-mouse IL-1R, Type I/p80 (clone JAMA-147)	Biolegend	Cat#113509; RRID: AB_2264757
PE anti-mouse α-SMA (clone E184)	Abcam	Cat#ab209435; RRID: AB_3065026
eFluor™ 660 anti-mouse Gata-3 (clone TWAJ)	eBioscience	Cat#50-9966-42; RRID: AB_10596663
PE anti-mouse T-bet (clone 4B10)	Biolegend	Cat#644810; RRID: AB_2200542
Brilliant Violet 421 ™ anti-mouse pSTAT3 (clone 13A3-1)	Biolegend	Cat#651010; RRID: AB_2572088
APC anti-mouse RORγt (clone B2D)	eBioscience	Cat#17-6981-82; RRID: AB_2573254
BV421 anti-mouse RORγt (clone Q31-378)	BD	Cat#562894; RRID: AB_2687545
Anti-human CD3	Invitrogen	Cat#MA512577; RRID: AB_10979571
Anti-human CD68	Bio-Rad	Cat#BX50031; RRID: AB_2936308
Anti-human CD127	Abcam	Cat#ab259806; RRID: AB_3065027
Anti-human CD20	Abcam	Cat#ab9475; RRID: AB_307267
Anti-human CD11c	Abcam	Cat#ab52632; RRID: AB_2129793
Anti-human MPO	Abcam	Cat#ab208670; RRID: AB_2864724
Anti-human PD-1	CST	Cat#43248S; RRID: AB_2728836
Anti-human CXCL16	R&D Systems	Cat#AF976; RRID: AB_355757
Anti-human/mouse CD3	Abcam	Cat#ab5690; RRID: AB_305055
Anti-human/mouse RORγt	eBioscience	Cat#14-6988-82; RRID: AB_1834475

REAGENT or RESOURCE	SOURCE	IDENTIFIER
Anti-human/mouse α-SMA-Cy3	Sigma-Aldrich	Cat#C6198; RRID: AB_476856
Anti-mouse PD-1	CST	Cat#84651S; RRID: AB_2800041
Anti-mouse CD127	eBioscience	Cat#14-1271-82; RRID: AB_467457
Anti-mouse CD3	Abcam	Cat#ab16669; RRID: AB_443425
Anti-mouse α-SMA	Abcam	Cat#ab32575; RRID: AB_722538
Anti-human/mouse JAK2 (phospho Y1007 + Y1008)	Abcam	Cat#ab32101; RRID: AB_775808
Anti-mouse IL-17A antibody	R&D Systems	Cat#MAB421-100; RRID: AB_2125018
Anti-mouse CXCL16 antibody	R&D Systems	Cat#MAB503-500; RRID: AB_2276752
Anti-mouse CD90.2	Bio X cell	Cat#BP0066; RRID: AB_1107682
Biological samples		
Human kidney biopsies	The First Affiliated Hospital, Sun Yat-sen University	N/A
Human periphery blood	The First Affiliated Hospital, Sun Yat-sen University	N/A
Chemicals, peptides, and recombinant proteins		
$NaHCO_3$	Macklin	Cat#S818079
Folic acid	Sigma-Aldrich	Cat#F8758
Recombinant mouse Angiotensin II	Sigma-Aldrich	Cat#A9525
DTT	Sigma-Aldrich	Cat#D9779-1G
Triton X-100	Sigma-Aldrich	Cat#T8787
Donkey serum	Sigma-Aldrich	Cat#D9663
DAPI	Sigma-Aldrich	Cat#D9542
RIPA	Sigma-Aldrich	Cat#R0278
DRAQ5	Abcam	Cat#ab108410
Stattic	Abcam	Cat#ab120952
Recombinant mouse IL-17A	R&D Systems	Cat#7956-ML-025
Recombinant mouse IL-23	R&D Systems	Cat#1887-ML-010
Recombinant mouse IL-1β	R&D Systems	Cat#401-ML-005
Collagenase type II	Gibco	Cat#17101015
Collagenase type I	Gibco	Cat#17100017
Dispase	Gibco	Cat#17105041
ACK solution	Gibco	Cat#A1049201
EDTA	Thermo Fisher	Cat#AM9260G
Ficoll	GE healthcare	Cat#17-1440-03
Cell Stimulation Cocktail	eBioscience	Cat#00-4975-93
NEOFECT DNA transfection reagent	NEOFECT	Cat#TF20121201
NP-40	Beyotime	Cat#BP0013
Protein A/G magnetic beads	MCE	Cat#HY-0202
Protease inhibitor cocktail	Roche	Cat#05892791001
Phosphatase inhibitor	Roche	Cat#4906845001

REAGENT or RESOURCE	SOURCE	IDENTIFIER
LightCycle 480 II	Roche	Cat#4887352001-p384
Enhanced chemiluminescence	Amersham Pharmacia Biotech	Cat# RPN2232
Critical commercial assays		
Human sCXCL16 ELISA kit	Abcam	Cat#ab187397
Mouse sCXCL16 ELISA kit	SAB	Cat#EK5311
RNeasy Mini kit	QIAGEN	Cat#74106
Fixation/Permeabilization kit	eBioscience	Cat#00-5523-00
Cell stimulation cocktail	eBioscience	Cat#00-4975-93
PANO 7-plex IHC kit	Panovue	Cat#0004100100
Transcriptor First Strand cDNA Synthesis Kit	Roche	Cat#4897030001
Multi Tissue dissociation kit	Miltenyi Biotec	Cat#130-110-201
Phire Tissue Direct PCR Master Mix	Thermo Fisher	Cat#F170S
Deposited data		
scRNA-seq data of intestinal and renal ILC3s	This paper	GSE249724
Experimental models: Cell lines		
HEK-293T	ATCC	CRL-3216
Experimental models: Organisms/strains		
Mouse: C57BL/6	Beijing Vital River Laboratory Animal Technology	Strain Number: 213
Mouse: B6.Cg-*Pdcd1*$^{tm1.1Shr}$/J	The Jackson Laboratory	JAX: 028276
Mouse: B6.129P2-*Rorc*^{tm1Litt}/J	The Jackson Laboratory	JAX: 007571
Mouse: B6.129P2(Cg)-*Rorc*^{tm2Litt}/J	The Jackson Laboratory	JAX: 007572
Mouse: B6.129P2-*Cxcr6*^{tm1Litt}/J	The Jackson Laboratory	JAX: 005693
Mouse: B6.FVB-Tg(Rorc-cre)1Litt/J	The Jackson Laboratory	JAX: 022791
Mouse: C57BL/6Smoc-*Pdcd1*$^{em1(flox)Smoc}$	Shanghai Model Organisms Center	NM-CKO-210063
Mouse: B6.129S7-*Rag1*^{tm1Mom}/J	The Jackson Laboratory	JAX: 002216
Mouse: B6.SJL-*Ptprc*^{a} *Pepc*^{b}/BoyJ	The Jackson Laboratory	JAX: 002014
Mouse: B6.Cg-c/c Tg(CAG-tdKaede)15Utr	RIKEN BioResource Center	RBRC No: RBRC05738
Oligonucleotides		
Primers for genotyping and real-time PCR, see Table S5–S6	This paper	N/A
Software and algorithms		
FlowJo	BD Biosciences	https://www.flowjo.com/
GraphPad Prism	GraphPad Software	https://www.graphpad.com
ImageJ	ImageJ	https://imagej.nih.gov/ij/
Biorender	Biorender	https://biorender.com
R studio	R studio	https://www.rstudio.com/
QuPath v0.2.0	QuPath	https://qupath.github.io
StrataQuest version 7.1.1.129	StrataQuest	https://www.tissuegnostics.cn/strataquest/